

Constraining modified gravity theories with scalar fields using black-hole images

Georgios Antoniou,^{1,2,*} Alexandros Papageorgiou,^{3,†} and Panagiota Kanti^{4,‡}

¹*Nottingham Centre of Gravity, Nottingham NG7 2RD, United Kingdom*

²*School of Mathematical Sciences, University of Nottingham,
University Park, Nottingham NG7 2RD, United Kingdom*

³*Center for Theoretical Physics of the Universe, IBS, 34126 Daejeon, South Korea*

⁴*Division of Theoretical Physics, Physics Department, University of Ioannina, GR 45110 Ioannina, Greece*

We study a number of well-motivated theories of modified gravity with the common overarching theme that they predict the existence of compact objects such as black holes and wormholes endowed with scalar hair. We compute the shadow radius of the resulting compact objects and demonstrate that black hole images such as that of M87* or the more recent SgrA* by the Einstein Horizon Telescope (EHT) collaboration may provide a powerful way to constrain deviations of the metric functions from what is expected from general relativity (GR) solutions. We focus our attention on Einstein-scalar-Gauss-Bonnet (EsGB) theory with three well motivated couplings, including the dilatonic and Z_2 symmetric cases. We then analyze the shadow radius of black holes in the context of the spontaneous scalarization scenario within EsGB theory with an additional coupling to the Ricci scalar (EsRGB). Finally, we turn our attention to spontaneous scalarization in the Einstein-Maxwell-Scalar (EMS) theory and demonstrate the impact of the parameters on the black hole shadow. Our results show that black hole imaging is an important tool for constraining black holes with scalar hair and, for some part of the parameter space, black hole solutions with scalar hair may be marginally favored compared to solutions of GR.

I. INTRODUCTION

Black holes, once considered as a mere mathematical curiosity of Einstein's General Theory of Relativity, are now known to populate our Universe in vast numbers. Currently, they are met at two different scales: stellar black holes with masses in the approximate range of $(5-70) M_\odot$ and supermassive black holes residing at the center of galaxies with masses as large as $10^{10} M_\odot$. A black hole is the most lucid manifestation of how gravity behaves at the strong regime and can thus serve as a test-bed for probing the fundamental theory of gravitational interactions.

Although General Relativity (GR) is a beautiful mathematical theory that has so far passed all experimental tests (see for instance [1–6]), it is clear that it cannot provide all the answers to several persisting, open questions in gravity and cosmology: the existence of singularities, the unknown nature of dark matter and dark energy, the difficulty in quantizing gravity and unifying it with the remaining forces in nature, to mention a few. The common consensus among scientists is that GR is only a low-energy limit of a more fundamental theory of gravity. As the structure of the final Quantum Theory of Gravity is still alluding us, the most usual approach taken in the meantime is that of the effective field theory: GR, a linear theory in terms of curvature, is now supplemented by higher gravitational terms, the presence of extra fields – mainly scalar and gauge fields – and new couplings including higher-derivative ones between matter and gravity.

Extending GR in this way unavoidably leads to a much richer range of gravitational solutions. To start with, new black hole solutions in the context of modified theories of gravity have long been known to exist [7–15] by evading the

no-hair theorems of GR [16–28] with a plethora of additional solutions having emerged during the last few years [29–51]. In addition, these modified theories predict also compact solutions other than black holes, such as traversable wormholes [52–73] and particle-like solutions [42, 74–80]. The exciting prospect of having our Universe populated also by these compact objects perhaps does not seem so unlikely nowadays.

Our first task, however, is to probe the validity of the modified gravitational theories predicting all these new gravitational solutions. The properties of the observed black holes or the observable signals from processes associated with black holes can serve as a valuable tool for this purpose. Indeed, the last few years we have witnessed the detection of gravitational waves from the merging processes of stellar black holes [81–83] but also the imaging observations of the supermassive black holes residing at the center of the M87 galaxy [84–91] and of our own Galaxy [92–97]. These observations have been used extensively in the literature to probe the validity of General Relativity and to set limits on modified gravitational theories (see, for example, [98–100]). Capturing the horizon-scale image of Sagittarius A* in particular, the supermassive black hole located in the center of our own Galaxy, presents a number of advantages. First, due to its proximity, the mass to distance ratio of Sagittarius A* is much more accurately determined than that of M87*. In addition, Sagittarius A* has a much smaller mass than M87*; this allows us to test a curvature scale which lies between the low curvature scale of the massive M87* black hole and the high curvature scale of stellar black holes.

The main feature in the horizon-scale images of the supermassive black holes is the bright photon ring which marks the boundary of a dark interior region, called the black-hole shadow [101]. The bright ring is formed by photon trajectories originating from parts of the universe behind the black hole which are gravitationally lensed by its gravitational field and directed towards our line of sight. These photons have impact parameters slightly larger than the ones which lead

* georgios.antoniou@nottingham.ac.uk

† papageo@ibs.re.kr

‡ pkanti@uoi.gr

to their capturing in bound, circular orbits around the black hole. The quantitative characteristics of the shadow can be calculated in the context of either GR or a modified theory of gravity and compared to the observed value, thus probing the validity of the theory in question.

In this work, we consider a set of modified gravitational theories with their common characteristic being the presence of a scalar field. This scalar field will be sourced by either gravitational terms, leading to induced or spontaneous scalarization, or gauge fields, leading to charged scalarized solutions. The presence of the scalar field modifies the gravitational background as well as the geodesic structure of the spacetime including the photon trajectories and the size and shape of the black-hole shadow. Employing the bounds on the deviation of the observed black-hole shadow of Sagittarius A* from that of the Schwarzschild solution¹, as these were derived by the Event Horizon Telescope [97] in a mass-scale independent form, we will examine the validity of a number of scalar-tensor and tensor-scalar-vector theories. In particular, we will consider the Einstein-scalar-Gauss-Bonnet (EsGB) theory with three different forms of coupling function between the scalar field and the GB term, a variant of the EsGB theory with an additional coupling between the scalar field and the Ricci tensor, and finally, the Einstein-Maxwell-scalar (EMS) theory with three different forms again of the coupling function between the scalar and the Maxwell fields. We demonstrate that the black-hole shadow bounds from Sagittarius A* can indeed impose restrictions on the parameter space or on the form of the coupling function of the scalar field in the aforementioned modified theories. However, the physical conclusions drawn depend very strongly on the particular EHT bound, or combination of EHT bounds, employed for this purpose. Thus, the use of individual bounds always allows ample parameter space where the majority of the modified theories considered are viable – in certain cases, they are even favoured compared to General Relativity. In contrast, demanding that all EHT bounds are simultaneously satisfied significantly reduces the parameter space and, at times, eliminates it.

The outline of the paper is as follows. In Section II we establish the notation and we provide a comprehensive review of the derivation of the bounds that quantify the deviation of the black hole shadow from the expected GR result. Next, in Section III we derive the connection between the metric components and the theoretically expected shadow radius in a model-independent way. We focus here on black holes and wormholes and demonstrate the differences of the shadows in each case. Subsequently in IV we initiate the main part of our work by demonstrating the bounds obtained by the EHT observations on EsGB theory with three distinct coupling functions. Next in Section V we turn our attention to some of the most well established models of spontaneous scalariza-

tion. Finally, in Section VI, we analyze the EMS theory and display the associated bounds. We outline our conclusions in Section VII.

II. THE EHT BOUNDS

The Event Horizon Telescope (EHT) is a Very Long Baseline Interferometry (VLBI) array with Earth-scale coverage [84–91]. It is observing the sky at 1.3 mm wavelength and has so far managed to provide the horizon-scale image of the two supermassive black holes located at the center of M87* and of our own Galaxy. The diameter \hat{d}_m of the bright photon ring surrounding the inner dark area – the most distinctive feature of these black-hole images – may be used to test theoretical predictions of both GR and modified theories. As noted above, in this work we will be using the horizon-scale image of Sagittarius A*. Following [97], one may write:

$$\hat{d}_m = \frac{\hat{d}_m}{d_{sh}} d_{sh} = \alpha_c d_{sh} = \alpha_c (1 + \delta) d_{sh,th}. \quad (1)$$

The diameter \hat{d}_m is the value of the diameter of the photon ring obtained by using imaging and model fitting to the Sagittarius A* data. The quantity α_c is a calibration factor which quantifies how accurately the ring diameter \hat{d}_m tracks the shadow diameter d_{sh} . It encompasses both theoretical and potential measurement biases and thus may be written as

$$\alpha_c = \alpha_1 \alpha_2 \equiv \left(\frac{d_m}{d_{sh}} \right) \left(\frac{\hat{d}_m}{d_m} \right). \quad (2)$$

Specifically, α_1 corresponds to the ratio of the true diameter of the peak brightness of the image (bright ring) d_m over the diameter of the shadow d_{sh} . If α_1 equals unity, the peak emission of the ring coincides with the shadow boundary. Its value depends on the specific black-hole spacetime and the emissivity model in the surrounding plasma. A large number of time-dependent GRMHD simulations in Kerr spacetime as well as analytic plasma models in Kerr and non-Kerr metrics lead to small positive values α_1 , namely $\alpha_1 = 1 - 1.2$. This result indicates that the radius of the brightest ring is always slightly larger than the black-hole shadow.

The second calibration parameter α_2 is the ratio between the inferred ring diameter \hat{d}_m and its true value d_m . Three different imaging algorithms were used in the measurement of the ring diameter \hat{d}_m denoted by *eht-imaging*, *SMILI* and *DIFMAP*, respectively [97]. The ring diameter was also determined by fitting analytic models, and more specifically the *mG-ring* model [95], to the visibility data. The three imaging methods led to a value of α_2 close to unity, while the *mG-ring* model allowed values of α_2 in the range (1-1.3).

Employing the above, the diameter of the boundary of the black-hole shadow may be written as $d_{sh} = \hat{d}_m / (\alpha_1 \alpha_2)$. Then, Eq. (1) allows us to solve for the fractional deviation δ between the inferred shadow radius $r_{sh,EHT}$ and that of a theory-specific black hole $r_{sh,th}$ [97]:

$$\delta = \frac{r_{sh,EHT}}{r_{sh,th}} - 1. \quad (3)$$

¹ Let us note that although we will make use of the bounds on the observed black-hole shadow from Sagittarius A* [97], our analysis will cover also the corresponding bound from the M87* observation [84–91, 98, 99] as the latter is less stringent and thus easier to satisfy.

Sgr A* estimates

		Deviation δ	1- σ bounds	2- σ bounds
<i>eht-imaging</i>	VLTI	$-0.08^{+0.09}_{-0.09}$	$4.31 \leq \frac{r_{\text{sh}}}{M} \leq 5.25$	$3.85 \leq \frac{r_{\text{sh}}}{M} \leq 5.72$
	Keck	$-0.04^{+0.09}_{-0.10}$	$4.47 \leq \frac{r_{\text{sh}}}{M} \leq 5.46$	$3.95 \leq \frac{r_{\text{sh}}}{M} \leq 5.92$
	Avg	$-0.06^{+0.064}_{-0.067}$	$4.54 \leq \frac{r_{\text{sh}}}{M} \leq 5.22$	$4.19 \leq \frac{r_{\text{sh}}}{M} \leq 5.55$
<i>SMILI</i>	VLTI	$-0.10^{+0.12}_{-0.10}$	$4.16 \leq \frac{r_{\text{sh}}}{M} \leq 5.30$	$3.64 \leq \frac{r_{\text{sh}}}{M} \leq 5.92$
	Keck	$-0.06^{+0.13}_{-0.10}$	$4.36 \leq \frac{r_{\text{sh}}}{M} \leq 5.56$	$3.85 \leq \frac{r_{\text{sh}}}{M} \leq 6.24$
<i>DIFMAP</i>	VLTI	$-0.12^{+0.10}_{-0.08}$	$4.16 \leq \frac{r_{\text{sh}}}{M} \leq 5.09$	$3.74 \leq \frac{r_{\text{sh}}}{M} \leq 5.61$
	Keck	$-0.08^{+0.09}_{-0.09}$	$4.31 \leq \frac{r_{\text{sh}}}{M} \leq 5.25$	$3.85 \leq \frac{r_{\text{sh}}}{M} \leq 5.72$
<i>mG-ring</i>	VLTI	$-0.17^{+0.11}_{-0.10}$	$3.79 \leq \frac{r_{\text{sh}}}{M} \leq 4.88$	$3.27 \leq \frac{r_{\text{sh}}}{M} \leq 5.46$
	Keck	$-0.13^{+0.11}_{-0.11}$	$3.95 \leq \frac{r_{\text{sh}}}{M} \leq 5.09$	$3.38 \leq \frac{r_{\text{sh}}}{M} \leq 5.66$
	Avg	$-0.15^{+0.078}_{-0.074}$	$4.03 \leq \frac{r_{\text{sh}}}{M} \leq 4.82$	$3.64 \leq \frac{r_{\text{sh}}}{M} \leq 5.23$

TABLE I. Sagittarius A* bounds on the deviation parameter δ . The colored bounds are the ones we use in the plots in the main part.

The above deviation parameter allows us to test the compatibility of the EHT measurements with GR or modified theories of gravity. The posterior over δ is obtained via the formula

$$P(\delta|\hat{d}) = C \int d\alpha_1 \int d\alpha_2 \int d\theta_g \mathcal{L}[\hat{d}|\alpha_1, \alpha_2, \theta_g, \delta], \quad (4)$$

$$\times P(\alpha_1)P(\alpha_2)P(\theta_g)P(\delta).$$

In the above, $\theta_g = GM/Dc^2$ is a characteristic angular size set by the black-hole mass and physical distance. Then, $\mathcal{L}[\hat{d}|\alpha_1, \alpha_2, \theta_g, \delta]$ is the likelihood of measuring a ring diameter \hat{d} , and $P(\theta_g)$ is the prior in θ_g . $P(\alpha_1)$ and $P(\alpha_2)$ are the distributions of the two calibration parameters and C a normalization constant.

To obtain the characteristic angular size θ_g of Sagittarius A* one needs its mass and distance. Two different instruments, the Keck Observatory and the Very Large Telescope together with the interferometer GRAVITY (VLTI), were used to study the orbits of individual stars around Sagittarius A*. The brightest star observed, S0-2, with a period of 16 years, has helped scientists to test relativistic effects such as gravitational redshift and the Schwarzschild precession [102–105] and to constrain alternative theories of gravity [106–108]. Its observation has also provided the most accurate so far measurements of the mass and distance of Sagittarius A*. The Keck team found for the distance a value of $R = (7935 \pm 50 \pm 32)\text{pc}$ and for the black hole mass the value $M = (3.951 \pm 0.047) \times 10^6 M_\odot$ [105]. The VLTI team found correspondingly $R = (8277 \pm 9 \pm 33)\text{pc}$ and $M = (4.297 \pm 0.012 \pm 0.040) \times 10^6 M_\odot$. Therefore, two different priors for θ_g were derived, namely $\theta_g = 4.92 \pm 0.03 \pm 0.01 \mu\text{as}$ (Keck) and $\theta_g = 5.125 \pm 0.009 \pm 0.020 \mu\text{as}$ (VLTI).

Employing these in Eq. (4), and assuming that the theory-specific solution considered in Eq. (3) is the Schwarzschild solution, for which it holds $r_{\text{sh,th}} = 3\sqrt{3}GM/c^2 = 3\sqrt{3}D\theta_g$, the corresponding values for the deviation parameter δ , along with their errors, were derived in [97] and are displayed in the

M87* estimates

		Deviation δ	1- σ bounds	2- σ bounds
EHT		$-0.01^{+0.17}_{-0.17}$	$4.26 \leq \frac{r_{\text{sh}}}{M} \leq 6.03$	$3.38 \leq \frac{r_{\text{sh}}}{M} \leq 6.91$

TABLE II. M87* bounds on the deviation parameter δ [99].

first column of Table I. We observe that the deviation δ always assumes negative values which means that the observed black-hole shadow is found to be smaller than the one predicted by GR for the Schwarzschild black hole. We also note that the value of δ derived by employing the measurements by VLTI is consistently more negative as compared to the one derived by Keck. The use of the specific algorithm for the image processing also affects the deviation parameter, with δ taking larger negative values as the *eht-imaging* algorithm is gradually replaced by the *SMILI*, the *DIFMAP* or the *mG-ring* algorithm. Finally, the value of δ is slightly modified by the type of simulations used in the calibration of α_1 ; here we employ the values obtained using the GRMHD simulations as an indicative case. We note, however, that all values derived for δ by EHT [97] are consistent with each other independently of the specific telescope, image processing algorithm or type of simulation used. For completeness, in Table II we present the corresponding value for the deviation parameter δ as derived by the black-hole image of M87* [99]; we observe that the central value of δ is much closer to zero but the errors are larger, due the larger uncertainty in the measurement of the mass and distance of M87*.

The definition of δ via Eq. (3) in conjunction with its values in the first column of Table I allows us to obtain the corresponding constraints on the dimensionless quantity r_{sh}/M (for notational simplicity, henceforth we drop the subscript EHT from the quantity $r_{\text{sh,EHT}}$). The 1- σ and 2- σ bounds on r_{sh}/M are displayed in the second and third column of Table I (and for completeness in the second and third column of Table II). We observe that, as expected, the constraints derived from Sagittarius A* are more stringent than the ones derived from M87*: the allowed range of values in the former case is always narrower and this leads to a consistently smaller upper limit of r_{sh}/M .

In this work, we will focus on two indicative sets of constraints, namely the ones obtained by using the *eht-imaging* method and the *mG-ring* analytic model, which lead to the smallest and largest δ (in absolute value), respectively. Moreover, in order to take a conservative stance, we will consider the Keck and VLTI values as independent and use their average value for δ ; these values together with the corresponding constraints on r_{sh}/M are displayed in the two rows of Table I denoted by the word "Avg". In Sections IV-VI, these mass-scale independent constraints will be used to test the viability of compact solutions arising in the context of modified gravitational theories with a scalar degree of freedom. Our analysis will pertain mainly to future observed black-hole shadow images and will act complementary to existing works placing bounds on the parameters of these modified gravitational theories.

We would like to finish this section with the following comment. Throughout this work, we will focus on spherically-symmetric solutions obtained in the context of the modified theories. It is for this reason that the theory-specific solution chosen above was the Schwarzschild solution and not the Kerr one. The rotation parameter and inclination angle of Sagittarius A* does affect the observed shadow radius. However, to our knowledge, at the moment there is no clear consensus on the value of these two parameters for Sagittarius A*. In addition, it was found [100] that the shadow radius is affected very little by the rotation of the compact object, independently of the inclination angle. In fact, a recent study [109] hints towards a rather small value of a_* , namely $a_* \leq 0.1$. In any case, it is estimated [97] that rotating black holes can have a shadow size which is smaller than that of a non-rotating black hole by up to 7.5%. Therefore, by considering the Schwarzschild solution as the theory-specific solution in our analysis seems to be a justified choice at the moment. In fact, due to the more compact geodesic structure of any rotating black hole compared to a non-rotating one, any "Schwarzschild" constraint applied in our analysis may be considered as the largest possible value for the corresponding "Kerr" one.

III. SHADOW RADIUS OF COMPACT OBJECTS

In this section, we present the analytic formalism which yields the expressions for the shadow radius of compact objects. As we argued above, the black-hole spin affects the shadow feebly. Therefore, we focus our analysis on solutions with spherical symmetry. First, we examine the case where the compact object is a black hole and then we consider the scenario where the compact object is a wormhole.

A. Black holes

We start by investigating the shadow size for a static and spherically symmetric configuration of the following form:

$$ds^2 = g_{tt} dt^2 + g_{rr} dr^2 + r^2 d\Omega^2. \quad (5)$$

We first need to locate the photon sphere for this background. To do that we consider the trajectory of a photon. Since spherical symmetry is assumed, we can consider, without loss of generality, motion on the equatorial plane $\theta = \pi/2$. The Killing vectors associated with the symmetries of this spacetime are $\xi_1^\mu = (1, 0, 0, 0)$ and $\xi_2^\mu = (0, 0, 0, 1)$. Then, following [110], we can define the 4-momentum of a photon as $\tilde{k} = (k^t, k^r, k^\theta, k^\varphi)$, with $k^\theta = 0$ (from symmetry arguments). Then, the conserved quantities, i.e. the energy and angular momentum are $E = -\xi_1^\mu k_\mu = -g_{tt} k^t$ and $L = \xi_2^\mu k_\mu = r^2 k^\varphi$, respectively. Moreover, the constraint $\tilde{k}^2 = 0$ fixes the k^r component of the 4-momentum, so that we may finally write:

$$\tilde{k} = \left(-\frac{E}{g_{tt}}, \sqrt{-\frac{E^2}{g_{tt} g_{rr}} - \frac{L^2}{g_{rr} r^2}}, 0, \frac{L}{r^2} \right). \quad (6)$$

It is now straightforward to locate the radius for circular photon orbits by demanding $k^r = 0$ and $dk^r/dr = 0$. In terms of the impact parameter $b \equiv L/E$, these conditions yield

$$b^2 = -\frac{r^2}{g_{tt}} \Big|_{r_{\text{ph}}} = -\frac{r^3 (g_{tt} g'_{rr} + g_{rr} g'_{tt})}{g_{tt}^2 (r g'_{rr} + 2g_{rr})} \Big|_{r_{\text{ph}}}, \quad (7)$$

which can be simplified to give the equation for the photon circular orbit radius

$$\text{Photon orbit radius: } r_{\text{ph}} = \frac{2g_{tt}}{g'_{tt}} \Big|_{r_{\text{ph}}}. \quad (8)$$

Our next step is to determine the shadow radius as observed by a far-away observer after lensing has been taken into account (see left plot of Fig. 1). For a null trajectory, we can write $g_{\mu\nu} \dot{x}^\mu \dot{x}^\nu = 0$, which in turn yields

$$g_{rr} \left(\frac{\dot{r}}{\dot{\varphi}} \right)^2 = -r^2 - g_{tt} \left(\frac{\dot{t}}{\dot{\varphi}} \right)^2, \quad (9)$$

where $E = -g_{tt} \dot{t}$ and $L = r^2 \dot{\varphi}$. Therefore, we can equivalently solve for the radial deviation with respect to the polar angle

$$\left(\frac{dr}{d\varphi} \right)^2 = -\frac{r^2}{g_{rr}} \left(\frac{r^2}{g_{tt} b^2} + 1 \right). \quad (10)$$

At the point of closest radial approach $r = r_0$, the equation above should vanish,

$$\frac{1}{b^2} = -\frac{g_{tt}}{r^2} \Big|_{r_0}. \quad (11)$$

From Fig. III A, we can also easily deduce that

$$\cot \alpha = \frac{\sqrt{g_{rr}}}{r} \frac{dr}{d\varphi} \Big|_{r_{\text{obs}}} \xrightarrow{(10)} \sin^2 \alpha = -\frac{g_{tt} b^2}{r^2} \Big|_{r_{\text{obs}}}. \quad (12)$$

Then, it is obvious that the angle for the shadow of the black hole is retrieved in the limit $r_0 \rightarrow r_{\text{ph}}$. We assume that asymptotically far away the spacetime is flat, therefore, $g_{tt} \rightarrow -1$. Then, for a far-away observer $\sin \alpha \approx \alpha$, so $\alpha_{\text{sh}} = b_{\text{crit}}/r_{\text{obs}}$, where b_{crit} is the value of the impact parameter given in Eq. (11) in the limit $r_0 \rightarrow r_{\text{ph}}$. From Fig. 1(a) and for $r_{\text{obs}} \gg r_{\text{ph}}$, we also have $\alpha_{\text{sh}} \approx r_{\text{sh}}/r_{\text{obs}}$. Identifying the two expressions for α_{sh} , we can finally deduce that

$$r_{\text{sh}} = b_{\text{crit}} = \frac{r_{\text{ph}}}{\sqrt{-g_{tt}(r_{\text{ph}})}}. \quad (13)$$

For a Schwarzschild black hole, for example, where $g_{tt} = -(1 - 2M/r)$, Eq. (8) readily gives $r_{\text{ph}} = 3M$. Employing this result in Eq. (13), we easily obtain that $r_{\text{sh}} = 3\sqrt{3}M$.

B. Wormholes

By employing a different spherically symmetric metric, we can study other types of compact objects which in fact exhibit

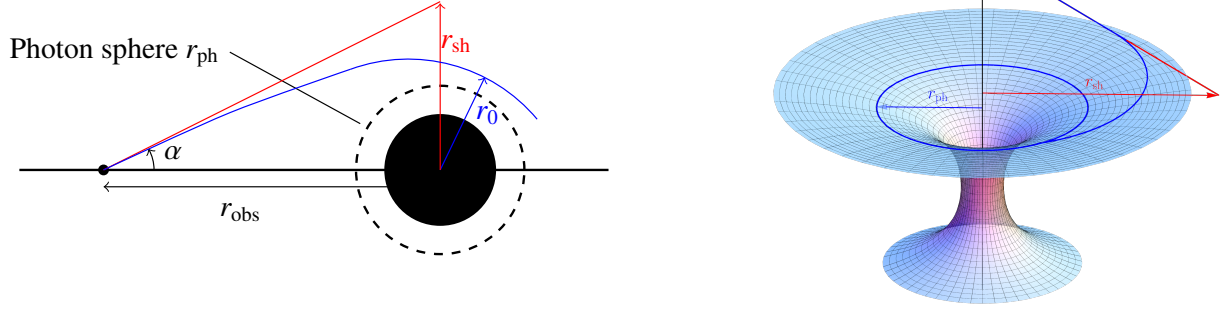


FIG. 1. *Left*: Qualitative representation of a light ray reaching an observer at an angle α , located at distance r_{obs} from the point singularity. The blue line traces a light ray escaping from a closed orbit around the black hole to infinity. The red line aligns with the inferred angle of approach for the light ray to an asymptotic observer. The point of closest approach for the light ray with respect to the black hole is located at $r = r_0$. If $r_0 = r_{\text{sh}}$ the light ray escapes the photon sphere. The shaded, circular area denotes the interior to the black-hole horizon, while the dashed, circular line corresponds to the location of the photon sphere. *Right*: Same but for a wormhole geometry. Here we show the embedding diagram depicting a finite radius throat along the vertical axis. The blue line traces a light ray escaping from the photon sphere to infinity, while the red straight line corresponds to the inferred line of approach to an asymptotic observer.

different shadow properties. Thus, we consider the following alternative form of line-element [64, 65, 111]

$$ds^2 = -e^{2\nu(l)} dt^2 + f(l) dl^2 + (l^2 + l_0^2) (d\theta^2 + \sin^2 \theta d\varphi^2), \quad (14)$$

which describes a wormhole geometry with a throat located at l_0 . In this spacetime, the conserved quantities are

$$E = -g_{tt}k^t = e^{2\nu} \frac{dt}{d\lambda}, \quad L = g_{\varphi\varphi}k^\varphi = (l^2 + l_0^2) \frac{d\varphi}{d\lambda}. \quad (15)$$

In order to find the photon sphere(s), we demand, as in the black-hole case, that $k^l = 0$ and $dk^l/dl = 0$. These yield the following equation which holds at the photon sphere(s):

$$v'(l_{\text{ph}}) = \frac{l_{\text{ph}}}{l_{\text{ph}}^2 + l_0^2}. \quad (16)$$

Upon solving this, we obtain the radii for the circular photon orbits in this background, namely

$$l_{\text{ph}} = \frac{1 \pm \sqrt{1 - 4l_0^2 v_{\text{ph}}'^2}}{2v_{\text{ph}}'}. \quad (17)$$

Also, for a null trajectory, we now find

$$\left(\frac{dl}{d\varphi}\right)^2 = \frac{(l^2 + l_0^2)}{f} \left[-1 + \frac{(l^2 + l_0^2)}{e^{2\nu} b^2}\right]. \quad (18)$$

In order to reach the point of the closest approach $l = l_c$, where the above equation vanishes, the impact parameter must assume the following value

$$b^2 = (l_c^2 + l_0^2) e^{-2\nu_c}. \quad (19)$$

For the wormhole background (14), the general equation (12) for the lensing takes the form

$$\cot \alpha = \sqrt{\frac{f(l)}{l^2 + l_0^2}} \frac{dl}{d\varphi} \Big|_{l_{\text{obs}}} \xrightarrow{(18)} \sin^2 \alpha = \frac{e^{2\nu} b^2}{l^2 + l_0^2} \Big|_{l_{\text{obs}}}. \quad (20)$$

For $l_{\text{obs}} \gg l_0, l_{\text{ph}}$, asymptotic flatness demands that $\nu \rightarrow 0$. The wormhole shadow is retrieved again in the limit $l_c \rightarrow l_{\text{ph}}$, for which $b \rightarrow b_{\text{crit}}$ according to Eq. (19). Thus, for a far-away observer, we obtain $a_{\text{sh}} \approx b_{\text{crit}}/l_{\text{obs}}$. But also, from Fig. 1(b), we find

$$a_{\text{sh}} \approx \frac{r_{\text{sh}}}{r_{\text{obs}}} \approx \frac{\sqrt{l_{\text{sh}}^2 + l_0^2}}{l_{\text{obs}}}, \quad (21)$$

where we have used the fact that the spacelike coordinate l is related to the radial coordinate r of the embedding diagram via the relation $l^2 = r^2 - l_0^2$. Thus, we can finally write

$$\sqrt{l_{\text{sh}}^2 + l_0^2} = b_{\text{crit}} = e^{-\nu(l_{\text{ph}})} \sqrt{l_{\text{ph}}^2 + l_0^2}. \quad (22)$$

One may apply the above formulae in the case of the Ellis-Bronnikov wormhole [112, 113] where $e^{2\nu} = f = 1$. Then, Eq. (17) gives $l_{\text{ph}} = 0$, and thus there is only one circular photon orbit located around the throat. Then, in the limit $l_c \rightarrow l_{\text{ph}}$, Eq. (19) yields that $b_{\text{crit}} = l_0$, and Eq. (20) takes the simplified form

$$\sin^2 \alpha = \frac{l_0^2}{l_{\text{obs}}^2 + l_0^2}, \quad (23)$$

which is exact and holds for all observers either far-away or close-by - this result is in agreement with Eq. (72) of [114]. Applying the result $b_{\text{crit}} = l_0$ also in Eq. (22), we obtain that $l_{\text{sh}} = 0$, or equivalently that $r_{\text{sh}} = l_0$. This behaviour is expected to change for wormhole spacetimes with a non-trivial g_{tt} metric component as in Eq. (14).

IV. THE EINSTEIN-SCALAR-GB THEORY

We initiate our analysis by considering a scalar-tensor theory which includes a quadratic gravitational term, the Gauss-Bonnet (GB) term defined as $\mathcal{G} = R_{\mu\nu\rho\sigma}R^{\mu\nu\rho\sigma} - 4R_{\mu\nu}R^{\mu\nu} + R^2$.

A general coupling function $f(\phi)$ between the scalar field ϕ and the GB term retains the latter – a topological invariant in four dimensions – in the theory. The action functional thus takes the following form

$$S = \frac{1}{2\kappa} \int d^4x \sqrt{-g} \left[R - \frac{1}{2} \nabla_\alpha \phi \nabla^\alpha \phi + f(\phi) \mathcal{G} \right]. \quad (24)$$

The resulting Einstein field equations and scalar field equation, after the variation of the above action with respect to the metric tensor and scalar field, are

$$G_{\mu\nu} = \frac{1}{2} \partial_\mu \phi \partial_\nu \phi - \frac{1}{4} g_{\mu\nu} \partial_\rho \phi \partial^\rho \phi - \frac{1}{2} (g_{\rho\mu} g_{\lambda\nu} + g_{\lambda\mu} g_{\rho\nu}) \eta^{\kappa\lambda\alpha\beta} \bar{R}_{\alpha\beta}^{\rho\sigma} \nabla_\sigma \nabla_\kappa f(\phi), \quad (25)$$

$$\nabla^2 \phi + \dot{f}(\phi) \mathcal{G} = 0, \quad (26)$$

respectively. In the second equation, the dot over the coupling function denotes its derivative with respect to the scalar field.

The EsGB theory has produced a large number of solutions describing compact objects with interesting characteristics: black holes with scalar hair [9–15, 29–51], traversable wormholes [56, 64, 65, 69] and particle-like solutions [42, 79, 80]. Here, we will focus mainly on the first class of solutions, namely black holes, and examine their viability under the light of the mass-scale independent constraints coming from the measurement of the shadow radius of Sagittarius A*. For the sake of comparison, we will briefly discuss also the viability of the dilatonic wormhole solutions postponing a more detailed analysis for a future work.

A. Black holes

The presence of the GB term in the action (24) causes the evasion of the scalar no-hair theorems and leads to the emergence of a large number of scalarized solutions, as mentioned above. In the context of the present analysis, we will consider spherically symmetric solutions that arise for three distinct coupling functions, namely for linear coupling (shift symmetry), quadratic coupling (Z_2 symmetry) and exponential coupling (dilatonic theory). The metric ansatz and field equations in explicit form may be found in Appendix A. For the details on constructing these solutions, the interested reader may consult [12, 38, 39, 115, 116].

In principle, our solutions require the specification of three parameters beyond GR. We need first to specify the coupling constant α which quantifies the strength of the interaction between the Gauss-Bonnet curvature invariant and the scalar field; we also need two boundary conditions for the scalar field, since it obeys a second order differential equation. Assuming a simple Taylor expansion of the scalar field around the horizon $\phi(r) = \phi_h + \phi_{h,1} (r - r_h) + \dots$, it has been shown in several works (see, for instance [12, 38]) that one may only obtain solutions with a regular horizon as long as the follow-

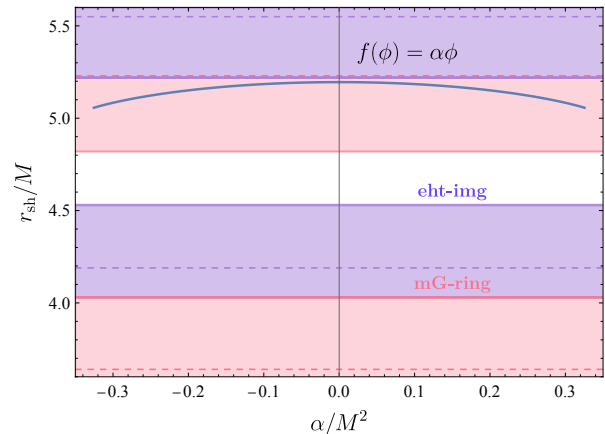


FIG. 2. Shadow radius for EsGB theory with a linear coupling.

ing constraint holds

$$\phi_{h,1} = -\frac{r_h}{4\dot{f}_h} \left(1 \mp \sqrt{1 - \frac{96}{r_h^4} \dot{f}_h^2} \right). \quad (27)$$

This reduces the parameters from three to two, namely the field value at the horizon ϕ_h and the coupling strength α . In addition to the preceding constraint, we also need to limit the two dimensional plane (ϕ_h, α) due to the requirement that the quantity under the square root in (27) is positive definite. For this reason, we will trade the parameter α with β defined as follows

$$\beta \equiv \frac{\sqrt{96}}{r_h^2} \dot{f}_h. \quad (28)$$

In this way, the parameter space we need to scan is (ϕ_h, β) with $-1 < \beta < 1$ defined within clear boundaries. After the study of the complete parameter space, our results will be eventually expressed again in terms of α .

1. $f(\phi) = \alpha \phi(r)$

For the case of the linear coupling, the two dimensional parameter space (ϕ_h, β) described above is reduced to one dimensional parameter space since the value of the field does not enter in the field equations as a result of the shift symmetry. In that case, the solutions are expected to form a line in the $(\alpha/M^2, r_{sh}/M)$ plane that spans the $-1 < \beta < 1$ parameter range.

This is indeed the case as seen in Fig. 2 where we depict the rescaled black-hole shadow r_{sh}/M in terms of the dimensionless parameter α/M^2 of the theory. We always choose positive values of ϕ so that the sign of the coupling parameter α directly reflects to the sign of β . Here, we consider both positive and negative values for α . Notice that the line of the solutions is mirror symmetric around the $\alpha = 0$ line. This is expected since the field equations as well as the initial conditions are symmetric under the simultaneous exchange of the

sign of $\dot{f} = \alpha$ and (ϕ', ϕ'') . This of course only holds for the linear coupling, for which $\ddot{f} = 0$.

We observe that the shadow radius r_{sh}/M decreases as α/M^2 increases. This is easily understood if we recall (see, for example [12, 38, 39, 111]) that the GB term causes a negative contribution to the total energy density of the theory and thus exerts a repulsive force. Therefore, if a black hole is to be created, any matter distribution needs to be compacted into a smaller area of spacetime compared to the case where the GB term is absent. As a result, the GB scalarized black holes have always a smaller horizon radius than e.g. the Schwarzschild black hole with the same mass [38, 39, 111]. Since the whole geodesic structure gets more compact as α increases, the shadow radius will also get smaller. This decreasing trend of the solution line holds for both $\alpha > 0$ and $\alpha < 0$ since the GB contribution to the energy density is negative independently of the sign of α . In fact, it is proportional to the combination $\phi_{h,1}\dot{f}_h$, which is always negative according to Eq. (27). This holds also independently of the exact form of the coupling function $f(\phi)$, and thus we expect to see a similar behaviour for the other two forms of f . We finally note that the solution lines abruptly terminate when the minimum mass solutions – another characteristic of the EsGB theory – are reached.

Let us now focus on the constraints imposed on the shift symmetric theory by the mass-scale independent bounds depicted in Table I. As explained in Section II, we will employ two of the derived bounds: the most ‘conservative’ bound, the *eht-imaging* one, which yields the smallest central value of the fractional deviation δ , and the most ‘liberal’ bound, the *mG-ring* one, which allows for larger deviations from GR. The two solid, horizontal, blue lines denote the allowed 1- σ range by the *eht-imaging* bound, while the two solid, horizontal, red lines denote the corresponding range allowed by the *mG-ring* bound (the blue and red horizontal, dashed lines denote the corresponding 2- σ bounds). Likewise, the blue-shaded area is the one excluded by the *eht-imaging* bound and the red-shaded area the one excluded by the *mG-ring* bound. The white area is the one which is allowed by both bounds.

According to Fig. 2, the complete range of scalarized solutions in the shift symmetric EsGB theory is compatible with the *eht-imaging* bound while it is altogether excluded by the *mG-ring* bound within 1- σ ! Our findings highlight in the best possible way the need to “bridge the gap” between the different EHT bounds as they lead to conflicting conclusions regarding the viability of certain solutions and, in a more general context, the physical relevance of their underlying theories. We note that all solutions found, which are allowed by the *eht-imaging* bound, satisfy also the recent experimental constraint on the dimensionless parameter $\alpha/M^2 < 0.54$ [117] set by the detection of gravitational waves by black-hole binaries. If, on the other hand, one takes a more conservative approach and demand that viable solutions should satisfy both of the EHT bounds, one is forced to exclude the complete range of scalarized, shift-symmetric solutions as none of them falls in the optimum white area of the plot.

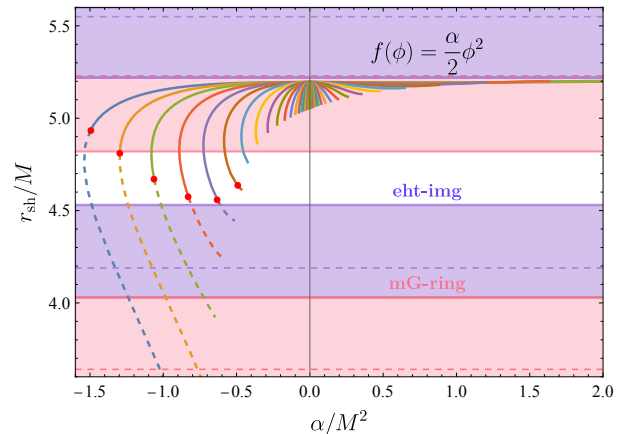


FIG. 3. Shadow radius for EsGB theory with a quadratic coupling.

$$2. \quad f(\phi) = \frac{\alpha}{2} \phi(r)^2$$

Unlike the linear case, the case of the quadratic coupling function necessitates searching along a two-dimensional parameter space due to the fact that the initial value of the field ϕ_h is physical. In order to facilitate the search, we select $N=25$ points equally spaced in $\ln(\phi_h)$ space with $\phi_{h,\text{min}} = 0.1$ and $\phi_{h,\text{max}} = 100$. For each of these N points, we scan the parameter space $-1 < \beta < 1$. The results are displayed in Fig. 3 where, for each choice of ϕ_h , we plot a line that spans the range $-1 < \beta < 1$. The red dots in the figure denote a transition point regarding the sign of T_r' near the horizon, which will be discussed shortly.

The lines in Fig. 3 denoting solutions with large ϕ_h are generally consolidated close to the vertical axis. In contrast, the smaller ϕ_h is, the more the lines spread out to larger values of $|\alpha/M^2|$. This is expected due to the definition of beta which in this case takes the form

$$\beta = \frac{\sqrt{96}}{r_h^2} \alpha \phi_h. \quad (29)$$

It is clear that in order to reach the values of $\beta \approx \pm 1$, i.e. the limits of the range of β , we need to choose an increasingly larger α in order to compensate for the smallness of ϕ_h . This justifies the fact that the lines extend further and further away from the origin for small ϕ_h values.

Additionally, one may observe that for negative values of the coupling constant α the mass parameter M is affected much more dramatically compared to the positive coupling case. This is manifested in Fig. 3 in the fact that the lines turn downward and to the right. This comes as a consequence of the dimensionless normalization we have applied to the axes. In addition to that, we have observed numerically that negative values of the coupling α lead to large and negative values of the scalar charge. The largeness of the charge and mass for values of the coupling deep into the negative regime is a generic consequence of the evolution of the field equations at intermediate scales between the horizon and infinity, and

hence it is difficult to understand the origin of this effect by studying the asymptotic behavior of the solutions.

Moreover, it is interesting to note that for some of the parameter space analyzed, one crosses the boundary beyond which one can obtain a solution with $\lim_{r \rightarrow r_h} T_r''(r) > 0$. We remind the reader that the condition $\lim_{r \rightarrow r_h} T_r''(r) < 0$ satisfied by the scalarized solutions found in [12, 38, 39] was employed to demonstrate the violation of the novel no-hair theorem [28]. Using the results of [116], we can compute the boundary beyond which solutions with $\lim_{r \rightarrow r_h} T_r''(r) > 0$ appear as follows

$$\lim_{r \rightarrow r_h} T_r''(r) = 0 \quad \Rightarrow \quad \alpha = -\frac{1}{4} + \frac{\beta^2}{16} - \frac{2\sqrt{1-\beta^2}}{9}. \quad (30)$$

Simultaneously, due to the definition of β , we can write

$$\alpha = \frac{r_h^2}{4\sqrt{6}\phi_h}\beta. \quad (31)$$

The above result implies that depending on the choice of ϕ_h and β , α can be above or below the boundary defined by (30). The points below the boundary, i.e. scalarized black-hole solutions with $\lim_{r \rightarrow r_h} T_r''(r) > 0$, are denoted by dashed lines in Fig. 3 and the transitioning points are marked by large red dots. We note that such solutions arise only in the case of negative coupling constant α , and thus any analyses considering only positive α are bound to overlook them.

Figure 3 leads to similar conclusions regarding the validity of the quadratic, scalarized GB solutions with positive α to the ones found for the linear-coupling case: the *eht-imaging* bound allows the complete range of solutions while the *mG-ring* bound excludes all of them within $1-\sigma$! No scalarized solutions with positive α fall in the white area. However, the situation is radically different for solutions with negative α . There, the lines of solutions with small or intermediate values of ϕ_h extend into the white area and thus survive all EHT bounds. These favoured solutions are characterised by either a positive or negative value of $\lim_{r \rightarrow r_h} T_r''(r) > 0$.

$$3. \quad f(\phi) = \alpha e^{\gamma\phi(r)}$$

For the dilatonic coupling, we need to scan a three dimensional parameter space since there is an additional parameter γ that characterizes the coupling function. We follow the same procedure as before, and display the results for two distinct values of $\gamma = 1, 2$ in Figs. 4 and 5, respectively.

The subclass of solutions derived for positive values of the coupling parameter α exhibit the same profile, for both values of γ , as in the previous two cases: the whole range of solutions are allowed by the *eht-imaging* bound but excluded by *mG-ring* bound within $1-\sigma$. No such solution manages to satisfy both bounds. In fact, all GB scalarized black holes derived for positive α demonstrate the same profile when it comes to their viability under the Sagittarius A* constraints independently of the particular form of the coupling function $f(\phi)$. We note again that all these solutions satisfy the theoretical bound $\alpha/M^2 < 0.69$, for the existence of scalarized dilatonic

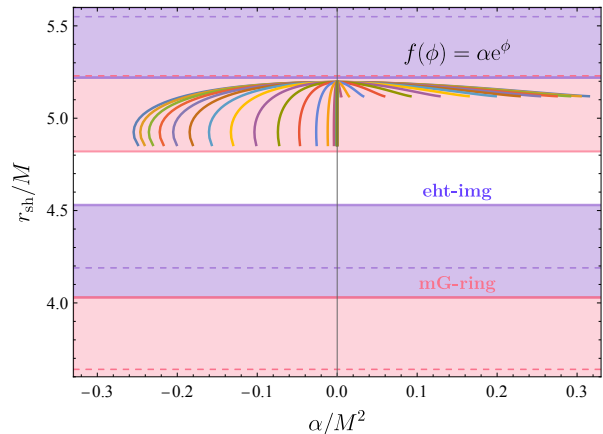


FIG. 4. Shadow radius for EsGB theory with a dilatonic coupling with $\gamma = 1$.

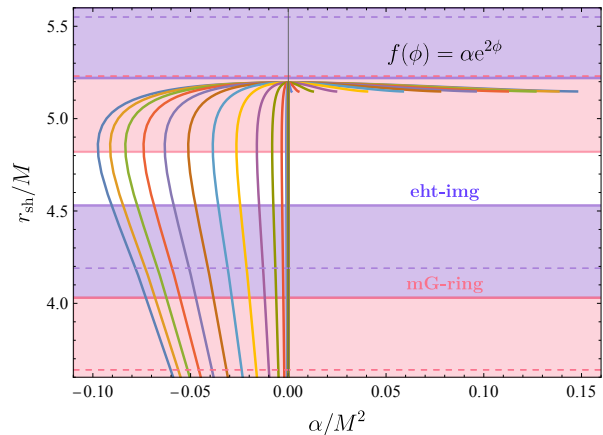


FIG. 5. Shadow radius for EsGB theory with a dilatonic coupling with $\gamma = 2$.

black holes [12, 30], and the experimental bound $\alpha/M^2 < 0.54$ [117].

The situation however is different when we consider the solutions derived for negative values of the coupling constant α . Considering also the behaviour observed in the previous two cases as well as the one depicted in Figs. 4 and 5, we conclude that this subclass of solutions is affected both by the form of the coupling function $f(\phi)$ and the particular values assumed for the parameters of the theory. In Fig. 4, we see that, for $\gamma = 1$, none of the negative- α solutions manages to satisfy both EHT bounds. However, for $\gamma = 2$, the solution lines extend across the white optimum area and thus a subgroup of solutions, for a very specific range of α , may be rendered viable. In this case, the only way to cross into the $\lim_{r \rightarrow r_h} T_r''(r) > 0$ regime for the dilatonic coupling is to increase the value of γ even further. However, this yields a less observationally motivated theory. Another important observation is that for the dilatonic coupling the ratio r_{sh}/M depends only on γ but not on α . This is due to the presence of a sym-

metry in the Lagrangian that allows us to absorb the constant $e^{\gamma\phi_0}$ into a redefinition of the coupling strength α [12].

B. Wormholes

In the context of the theory (24), traversable wormhole solutions have been discovered for a variety of scalar-GB couplings, featuring single or double-throat geometries [64, 65, 111]. Exploring these solutions in depth is beyond the scope of this work and is left for future analysis. Here, however, we will present the results for one characteristic example in order to demonstrate the potential of our analysis as a tool to observationally distinguish wormhole from black-hole solutions.

The case we consider here is the first one historically studied [64, 65] and involves an exponential coupling function of the form $f(\phi) = \alpha e^{-\gamma\phi}$ with $\gamma = 1$. Single throat solutions are then discovered if one assumes the line element given in (14). In accordance with the black-hole scenario a regularity for the scalar field's derivative on the throat is derived

$$\phi_0'^2 = \frac{f_0(f_0 - 1)}{2\alpha e^{-\phi_0} \left[f_0 - 2(f_0 - 1) \frac{\alpha}{f_0} e^{-\phi_0} \right]}, \quad (32)$$

where f_0 and ϕ_0 are the values of f and ϕ evaluated at the throat. For simplicity here, we chose ϕ_0 so that asymptotically the field vanishes. Additionally, the value of the other metric function v_0 at the throat is chosen so that an asymptotically flat spacetime is recovered. We are left therefore with one free parameter, i.e. f_0 , in addition to the coupling one.

In the limit $f_0 \rightarrow 1$ the redshift function v_0 tends to larger negative values and a horizon emerges, thus yielding the relevant black-hole solutions in this theory. This allows us to directly compare the shadow radii between black holes and wormholes arising for $\gamma = 1$. The results are presented in Fig. 6, where we see that f_0 has non-trivial consequences both on the shadow radius and on the mass range of the solutions. Specifically, it appears that as we increase f_0 the mass range

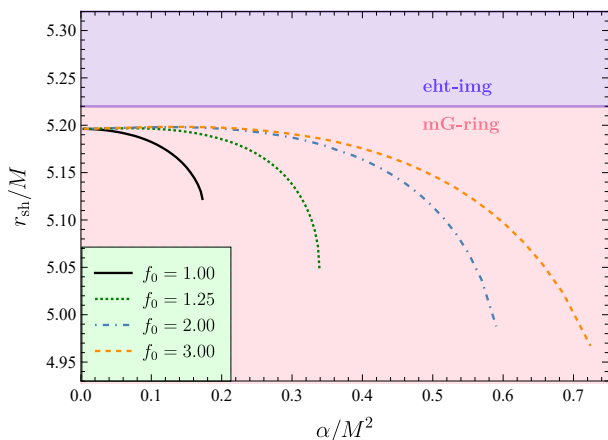


FIG. 6. Wormhole solutions in EsGB theory with coupling function $f(\phi) = \alpha e^{-\phi}$, for $f_0 = \{1, 1.25, 1.5, 2, 3\}$.

can also increase significantly. In terms of the shadow radius, we see that all solutions -including the black hole- presented lay within the averaged $1-\sigma$ *eht-imaging* bounds presented in Table I. On the other hand, all solutions are excluded within $1-\sigma$ if one chooses to consider the averaged *mG-ring* estimates. Once again, no solution exists that satisfies both bounds.

V. CURVATURE-INDUCED SPONTANEOUS SCALARIZATION

A particular class of scalar-tensor theories, in the more general framework of Horndeski theory, has attracted a lot of attention and has been extensively scrutinized over recent years. This class pertains to a phenomenon known as *spontaneous scalarization* of compact objects (black holes and neutron stars). It describes solutions *spontaneously* endowed with scalar hair as a consequence of a "phase transition" associated with the emergence of a tachyonic instability. Beyond a certain compactness threshold, black holes tend to transition from unstable, unscalarized GR solutions to stable scalarized configurations. The main reason why this particular class of theories entails exceptional interest relates to the fact that GR is retrieved in the weak gravitational-field regime, while deviations are only detected in heavily curved spacetimes.

The initially theorized model [40, 41] considered GR supplemented by a kinetic term for the scalar field plus a non-minimal interaction of the scalar field with the GB invariant. For spontaneous scalarization to be realised, it is crucial that this coupling satisfies a certain number of conditions, which will be discussed in the following paragraphs. However, this initial model has been shown to be unstable under radial perturbations [118, 119].

Following arguments discussed in detail in [120], we can write a general action allowing for spontaneously scalarized solutions to emerge, in the following form:

$$S = \frac{1}{2\kappa} \int d^4x \sqrt{-g} \left[R - \frac{1}{2} \nabla_\alpha \phi \nabla^\alpha \phi + h(\phi)R + f(\phi)\mathcal{G} + V(\phi) \right], \quad (33)$$

where \mathcal{G} is again the Gauss-Bonnet invariant. The scalar field self-interactions have been shown to non-trivially affect the properties of the scalarized solutions. This includes the threshold of scalarization which is altered by the bare mass term, and the radial stability which is improved if one includes quartic interactions [47]. Here we consider $V(\phi) = 0$. Another way to stabilize black-hole solutions in this theory is to include higher order operators in the GB coupling function $f \sim \alpha\phi^2 + \zeta\phi^4$. Provided that ζ is a large enough negative multiple of α , solutions can indeed be stabilized [121].

The field equations for the metric that one derives by varying the action (33) are:

$$G_{\mu\nu} = T_{\mu\nu}^\phi, \quad (34)$$

where the scalar-field energy-momentum tensor is given by:

$$T_{\mu\nu}^{\phi} = \frac{1}{2} \nabla_{\mu} \phi \nabla_{\nu} \phi - \frac{1}{4} g_{\mu\nu} (\nabla \phi)^2 - (g_{\mu\nu} \nabla^2 - \nabla_{\mu} \nabla_{\nu}) h(\phi) - h(\phi) G_{\mu\nu} - \frac{1}{g} g_{\mu(\rho} g_{\sigma)\nu} \epsilon^{\kappa\rho\alpha\beta} \epsilon^{\sigma\gamma\lambda\tau} R_{\lambda\tau\alpha\beta} \nabla_{\gamma} \nabla_{\kappa} f(\phi). \quad (35)$$

Since in this work we assume spherical symmetry, we must recover the Schwarzschild geometry asymptotically. Perturbing the scalar equation around the GR solution ($\phi = \phi_0 + \delta\phi$), we find:

$$\square\phi = - [f'(\phi)\mathcal{G} + h(\phi)R] \Rightarrow \square\delta\phi = -\dot{f}'(\phi_0)\mathcal{G}\delta\phi. \quad (36)$$

The term $-\dot{f}'(\phi_0)\mathcal{G}$ acts as an effective mass for the scalar field, therefore, when it becomes significantly negative, it triggers a tachyonic instability. The first spontaneous scalarization condition therefore requires $\dot{f}'(\phi_0)\mathcal{G} > 0 \Rightarrow \dot{f}'(\phi_0) > 0$, since $\mathcal{G} > 0$ in the exterior of spherically symmetric black holes. If we also integrate the scalar equation by parts, it is straightforward to show that for spontaneously scalarized black holes to emerge it is also required that $\phi f(\phi) > 0$. The second condition is that the coupling function should satisfy relates to GR being included in this framework, i.e. $f(\phi_0) = 0$ for some ϕ_0 .

The scalarization occurs beyond a threshold mass which is found by examining the linear stability of scalar perturbations around the Schwarzschild background. To that extend the scalar perturbation is decomposed as follows

$$\delta\phi = \frac{\sigma(r)}{r} Y_{\ell}^m(\theta, \phi) e^{-i\omega t}, \quad (37)$$

where $Y_{\ell}^m(\theta, \phi)$ are the spherical harmonics. For spherical symmetry, the above yields an equation of the following type:

$$\frac{d^2\sigma}{dr^2} + \omega^2\sigma = V_{\text{eff}}(\ell, \alpha)\sigma. \quad (38)$$

The effective potential depends on the theory, and α corresponds to the coupling parameter appearing within $f(\phi)$. Requiring the existence of bound solutions to the above equation that satisfy the proper asymptotic properties (equivalence with square integrability in quantum mechanics), allows us to determine the discrete spectrum of scalarization thresholds depending on the mode n , and the angular number l . For a massless scalar field with $\ell = 0$, the thresholds for the fundamental mode and the first overtone are found to be $\hat{M}_{\text{th}}^{(0)} \approx 1.179$ and $\hat{M}_{\text{th}}^{(1)} \approx 0.453$, respectively. Here, and in what follows, we have defined the dimensionless mass parameter

$$\hat{M} = M_{\text{ADM}}/\alpha^{1/2}, \quad (39)$$

where M_{ADM} is the ADM mass of the solution which is read off the asymptotic expression of g_{rr} . This is done so that our results are directly comparable with the existing bibliography.

In the next two subsections, we address two particular models, the *minimal model* characterised by coupling functions of quadratic form and the *quartic sGB model* where the coupling function to the GB term has been supplemented by a quartic function of the scalar field.

A. Minimal model

Here, we consider the minimal model associated with spontaneous scalarization identified in [120] and explored in [119, 122–125], where the coupling functions are defined as

$$h(\phi) = -\frac{\beta}{2}\phi^2, \quad f(\phi) = \frac{\alpha}{2}\phi^2, \quad (40)$$

where β and α are coupling constants. This subclass of scalarization models has particular interest as it addresses a number of issues traditionally associated with scalarization. Specifically: (i) it suppresses neutron-star scalarization leading to avoidance of binary pulsar constraints [124], (ii) it allows for a late time cosmological attractor to GR [123], (iii) it yields stable scalarized black-hole solutions [119, 125], and (iv) it improves the hyperbolicity of the formulation [119]. Considering the various benefits of this sRGB synergy, here we try to test its implications to black-hole shadows.

To this end, in Fig. 7 we present the shadow radius for spontaneously scalarized black-hole solutions derived for different values of the scalar-Ricci coupling constant β . In terms of cosmological consistency, it has been pointed out that negative β values require substantial fine tuning if one wants to retrieve a late-time attractor. This fine-tuning, however, is not required when $\beta > 0$, when a GR attractor is naturally recovered at late times. Therefore, we will be considering only positive values for β in what follows. Positive values of β have also been shown to improve the hyperbolic formulation of the scalar perturbations equation [119]. Also, changing the value of β has been shown to change the gradient of the curves in the scalar charge-mass plots, a relation directly associated with the stability of the solutions [121, 125]. A positive/negative gradient describes unstable/stable solutions. In general we can distinguish between three regions: (I) $\beta \lesssim 1$ solutions are unstable, (II) $1 \lesssim \beta \lesssim 1.2$ the solution curves have both a stable and an unstable part (effectively yielding one stable and one unstable solution for any \hat{M}), and (III) $\beta > \beta_{\text{crit}} \approx 1.2$ when all solutions are stable. Finally, values of β close to one achieve scalarization suppression for neutron stars [124] and avoid significantly influencing the formation of Large Scale Structures.

However, here we aim at conducting a comprehensive study and thus, in Fig. 7, we present the results for the radius of the black-hole shadow in the minimal model for a variety of values of β , namely $\beta = \{0, 5, 10, 50, 100\}$. The left panel depicts the solutions for the fundamental mode ($n = 0$). Here, the case $\beta = 0$, shown with a solid red line, corresponds to the radially unstable sGB scalarization model. The solutions in this case lie to the right of the scalarization threshold at $\hat{M}_{\text{th}}^{(0)} \approx 1.179$. The rest of the curves shown correspond to values of β that are larger than the critical value and therefore to stable configurations. The right panel shows the solutions for the first overtone ($n = 1$). Here, only the solutions with $\beta \gtrsim 10$, which lie to the left of the threshold scalarization value of $\hat{M}_{\text{th}}^{(0)} \approx 0.453$, are stable. In both plots, the horizontal axis depicts the value of the dimensionless parameter \hat{M} defined in Eq. (39). The vertical axis showing the shadow radius r_{sh} of the black hole is also properly re-scaled in terms of the mass

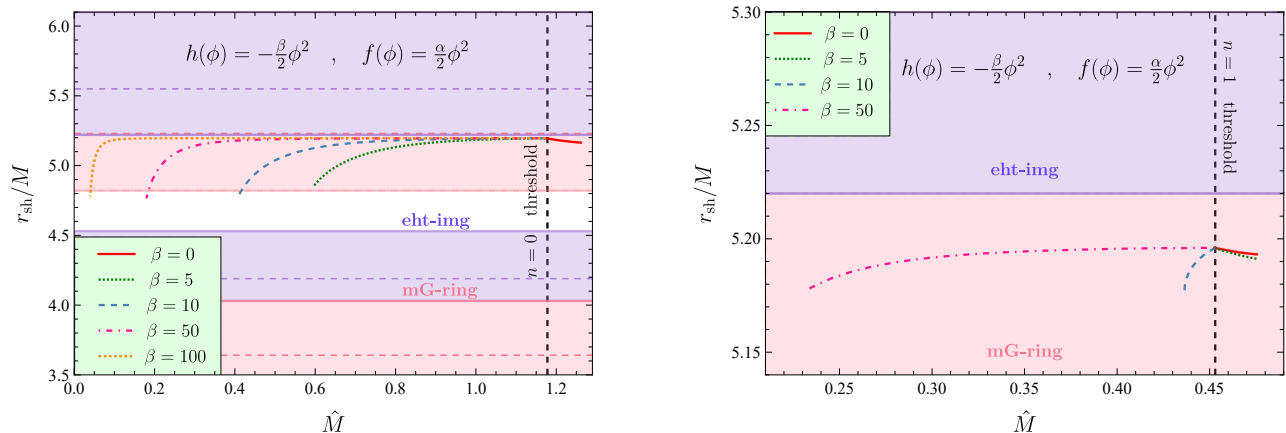


FIG. 7. *Left*: Shadow radius of the fundamental mode ($n = 0$) for spontaneously scalarized black holes in the EsRGB theory with quadratic couplings between the scalar field and curvature. The values of the ϕ - R coupling for the lines plotted are $\beta = 0, 5, 10, 50, 100$. At the same time the ϕ - \mathcal{G} coupling spans all the allowed values for which spontaneously scalarized solutions are retrieved. *Right*: Same as left panel but for the first overtone $n = 1$. The $\beta = 100$ case is not presented here for illustrative purposes as it extends to values of \hat{M} that are much smaller than the rest.

M so that the results are independent of the black-hole mass under consideration.

We readily observe that significant deviations from GR appear in the value of the shadow radius especially towards the lower mass limit of each curve. This is to be expected since it is for the lightest black holes that the curvature is stronger and the effect of both the GB and additional Ricci term becomes increasingly more important. As in the EsGB theory, the quadratic GB term leads to black holes with a more compact geodesic structure, compared to the Schwarzschild solution with the same mass, with the radius of the black-hole shadow following along and taking smaller values, too. The more conservative *eht-imaging* bound allows all of the solutions to 1- σ accuracy, whereas the *mG-ring* bound, which favours larger deviations from GR, excludes almost all of the solutions to 1- σ accuracy. The only solutions allowed are the ones towards the bottom tip of the curves for the fundamental modes. Considering the *mG-ring* 2- σ bounds however all solutions are allowed.

Therefore, if future observations of horizon-scale images of much lighter black holes are made with the same error bounds, scalarized black-hole solutions would be either favoured or even admitted as the only possible choice compared to the GR solution. Focusing on the character of Sagittarius A*, though, spontaneous scalarization may not be a viable option: all stable solutions arise in the regime $\hat{M} < 1.2$, which translates to $0.7 < \alpha/M^2$. If, in addition, we focus on the subclass of solutions which survive both the *eht-imaging* and the *mG-ring* bounds, these emerge for $\beta \gtrsim 7$ in the regime $\hat{M} < 0.5$ or for $4 < \alpha/M^2$. At the moment, there are no bounds on the dimensionless parameter $\zeta \equiv \alpha/M^2$ derived in the context of the EsRGB theory. However, if we take the theoretical bound $\zeta < 0.69$, for the existence of dilatonic black holes [12, 30], or the experimental bound $\zeta < 0.54$ [117] for shift symmetric solutions as indicative values, we see that the aforementioned range significantly surpasses the latter ones. A more detailed

study dedicated to the EsRGB theory needs to be performed before concluding whether Sagittarius A* is a spontaneously scalarised black-hole solution.

B. Quartic sGB coupling

Here we examine a variation of the EsGB model (without the Ricci coupling) that has been shown to yield stable black-hole solutions under certain assumptions [121]:

$$h(\phi) = 0 \quad , \quad f(\phi) = \frac{\alpha}{2}\phi^2 + \frac{\zeta}{4}\phi^4. \quad (41)$$

As mentioned earlier, for sufficiently negative values of the ratio $\zeta/\alpha \lesssim -0.7$, black holes do get stabilized. Considering positive ratios, on the other hand, produces solutions that are unstable. As in the minimal model, there is a particular range of negative values for the ratio ζ/α for which both stable and unstable solutions emerge.

One of the reasons why this model is particularly interesting relates to the fact that even for small values of the quartic coupling, the minimum mass can in principle be pushed to very small values, contrary to the minimal model presented in the last subsection. This feature has evaded attention in other works and is of significant importance as it allows us to probe a much larger range of masses. A consequence of this large mass range is an equally large range in the shadow radii as can be seen in Fig. 8. It is important to mention that the minimal mass for any $\zeta/\alpha \lesssim -0.7$ seems to have the potential to be arbitrarily pushed to small values.

Employing the mass-scale independent bounds of Table I, we may draw a number of useful conclusions. To start with, solutions with fairly large, negative values of ζ/α , i.e. $\zeta/\alpha \simeq -10$, seem to be excluded by the *mG-ring* bound, at least in the intermediate and larger mass regime. For less negative values of ζ/α the region allowed by the bounds from Table I

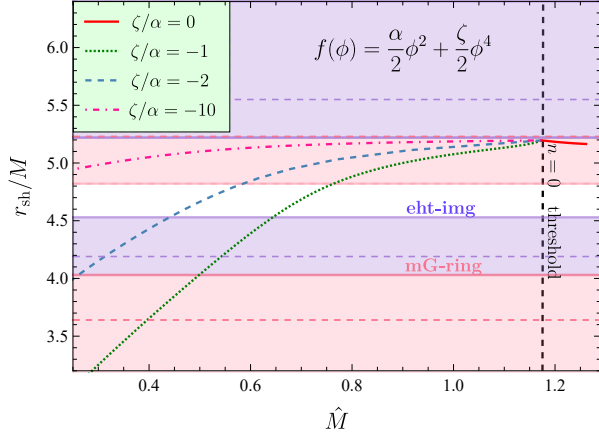


FIG. 8. Shadow radius of the fundamental modes ($n = 0$) for spontaneously scalarized black holes in EsGB theory with a quartic ϕ - \mathcal{G} coupling, for different ratios $\alpha/\zeta = \{0, -1, -2, -10\}$.

is pushed to intermediate masses. In general, for some fixed ζ/α , solutions with large masses tend to be disfavoured by the *mG-ring* bound while small-mass solutions are excluded by the *eht-imaging* bound, and this holds independently of the value of that ratio.

We note that, in this case, the solutions which are allowed by the existing bounds of Table I emerge for $\hat{M} < 0.85$ or for $1.4 < \alpha/M^2$. This is an improvement since the lower bound on α/M^2 is now much closer to the indicative theoretical and experimental bounds mentioned earlier. Again, in the absence of a bound on α/M^2 specifically for the quartic EsGB model, we cannot conclusively state whether Sagittarius A* can be a spontaneously scalarized solution arising in the framework of this model.

VI. THE EINSTEIN-MAXWELL-SCALAR THEORY

In the black-hole scenario there exists a wider class of theories that also includes Einstein-Maxwell-scalar (EMS) models as spontaneous-scalarization frameworks [126]. The EMS model describes a scalar field non-minimally coupled to Maxwell's tensor, while being minimally coupled to gravity. It has been shown that under certain assumptions black-hole solutions appear to spontaneously scalarize [126–128]. For small values of charge to mass ratio q , these solutions have been demonstrated to be the endpoints of a dynamical evolution of unstable Reissner–Nordström (RN) solutions with the same q within numerical error, while for larger values dynamical scalarization decreases its value. The action functional describing the EMS theory is given by:

$$S = \frac{1}{2\kappa} \int d^4x \sqrt{-g} \left[R - \frac{1}{2} \nabla_\alpha \phi \nabla^\alpha \phi + f(\phi) F_{\mu\nu} F^{\mu\nu} \right]. \quad (42)$$

The theory we consider here admits the RN solution which is scalar free. To accommodate this we require that asymptoti-

cally our theory must approach the RN solution, which translates to $\phi \rightarrow 0$ and $f(\phi) \rightarrow -1$, as $r \rightarrow \infty$.

The Einstein, Maxwell and scalar field equations are produced by variation with respect to the metric tensor, the electromagnetic tensor and the scalar field respectively, and they read

$$G_{\mu\nu} = T_{\mu\nu}, \quad (43)$$

$$\square\phi + \dot{f}(\phi) F_{\mu\nu} F^{\mu\nu} = 0, \quad (44)$$

$$\partial_\mu \left(\sqrt{-g} f(\phi) F^{\mu\nu} \right) = 0, \quad (45)$$

where the energy-momentum tensor contains contributions from the scalar and electromagnetic field:

$$T_{\mu\nu} = -\frac{1}{4} g_{\mu\nu} (\nabla\phi)^2 + \frac{1}{2} \nabla_\mu \phi \nabla_\nu \phi + f(\phi) \left[\frac{1}{2} g_{\mu\nu} F_{\rho\sigma} F^{\rho\sigma} - 2g^{\rho\sigma} F_{\mu\rho} F_{\nu\sigma} \right]. \quad (46)$$

As in the curvature-induced scenario, for the model to be continuously connected to GR, the property $\dot{f}(\phi_0) = 0$ should be satisfied for some ϕ_0 . The coupling functions which we will consider here satisfy the aforementioned properties and are given by

$$f_e(\phi) = -e^{-\alpha\phi^2}, \quad (47)$$

$$f_q(\phi) = -1 + \alpha\phi^2, \quad (48)$$

$$f_h(\phi) = -\cosh(\sqrt{-2\alpha}\phi), \quad (49)$$

where the coupling constant α is negative. In this case, by taking perturbations of the scalar equation around a RN background, we find that the requirement for the emergence of a tachyonic instability is equivalent to the condition $\dot{f}(\phi_0) F^2 > 0$. Here, we consider a purely electric field, namely:

$$A_\mu dx^\mu = V(r) dt \Rightarrow F_{\mu\nu} F^{\mu\nu} < 0, \quad (50)$$

which in turn requires $\dot{f}(\phi_0) < 0$. If we also integrate by parts, a second condition is derived, namely $\phi \dot{f}(\phi_0) < 0$.

In order to demonstrate the dependence of the shadow radius on the parameters of the theory, we fix α to different negative values and allow for our code to scan the parameter space for the values of $q \equiv Q_e/M$, where Q_e is the electric charge, for which scalarized solutions exist. The existence line for scalarization is presented in the top left panel of Fig. 9. To create this plot, we examine the linear stability of scalar perturbations around the RN background. We decompose the field perturbation as was described in Eq. (37) and we follow the same procedure. Following this method, we determine the scalarization thresholds for the first three modes, i.e. for $n = 0$, $n = 1$ and $n = 2$. This yields the minimum value of $|\alpha|$ for a fixed value of q for which we expect spontaneous scalarization to occur. This value appears to be increasing as one increases n . It is worth-pointing out that since the threshold of scalarization corresponds to small values of ϕ , it is independent of our choices of the coupling function accounting for the fact that all of them become identical for small ϕ .

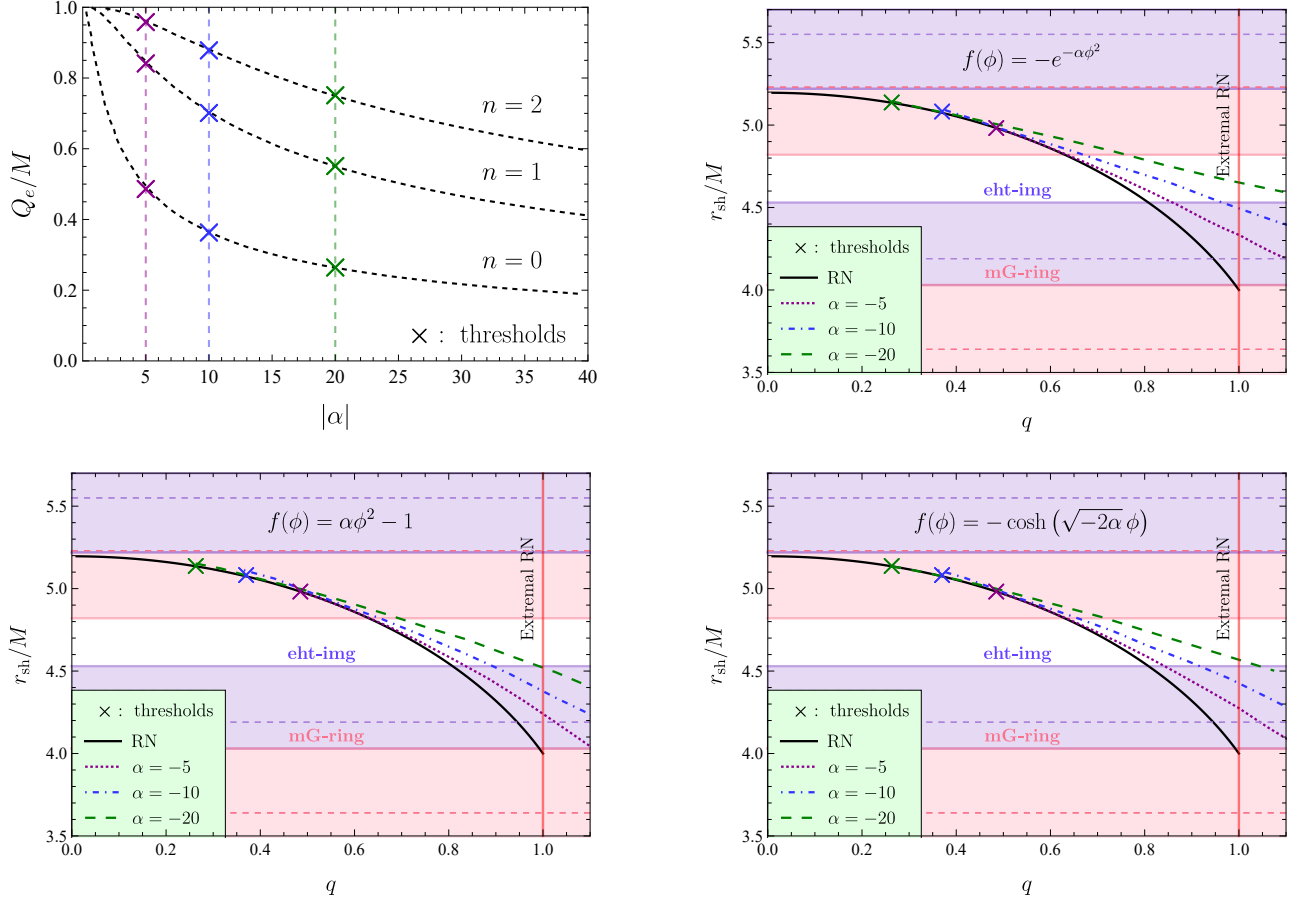


FIG. 9. *Top Left*: Onset of scalarization for different overtone numbers. The threshold does not depend on the coupling function. *Top Right*: Shadow radius for the fundamental mode for spontaneously scalarized EMS black holes with an exponential coupling function $f(\phi) = -e^{-\alpha\phi^2}$, for an s-EM coupling with values $\alpha = \{-5, -10, -20\}$. The solid line corresponds to the GR limit (RN). *Bottom Left*: Same as top right but for a quadratic coupling function $f(\phi) = \alpha\phi^2 - 1$. *Bottom right*: Same as top right but for a hyperbolic coupling function of the form $f(\phi) = -\cosh(\sqrt{-2\alpha}\phi)$.

In the remaining three panels of Fig. 9, we present the rescaled black-hole shadow r_{sh}/M in terms of q for the three coupling functions given in Eqs. (47)-(49). The scalarized solutions depicted refer to the fundamental mode of the scalar field with $n = 0$ and $\ell = 0$. The black solid line in each of the three plots corresponds to the shadow radius for RN black holes with different parameters q . The value of it can be found analytically to be:

$$\frac{r_{\text{sh}}}{M} = \frac{\sqrt{9 - 8q^2} + 3}{\sqrt{2 + (\sqrt{9 - 8q^2} - 3)/(2q^2)}}. \quad (51)$$

The coloured lines correspond to solutions with a different value for the EMS coupling, namely $\alpha = \{-5, -10, -20\}$. The "x" symbol appearing in each coloured line corresponds to the scalarization threshold for each α . For all three choices of the coupling function we observe similar results: First, the extremality limit can be exceeded for scalarized solutions, i.e. solutions with $q > 1$ emerge. Second, the charge range appears to increase the more we increase the absolute value of

the coupling parameter. This confirms the results appearing in [126–128].

The latter result effectively means that a larger domain in the parameter space of q allows for solutions with a shadow radius lying within the desired bounds. Indeed, as we observe from the three plots of Fig. 9 for the three different forms of the coupling function, an increase in $|\alpha|$ decreases the slope of each solution line and thus increases the range of solutions which fall in the white area. These solutions satisfy again all bounds of Table I coming from the Sagittarius A* constraints. The more ‘conservative’ bound, the *eht-imaging* one, clearly favours solutions with small and up to intermediate values of q . On the other hand, the more ‘liberal’ bound, the *mG-ring* one, tends to favour solutions with intermediate and large values of the charge parameter including the ones beyond RN extremality. According to these results, charged scalarized solutions can be viable candidates for future-observed black holes. However, on the average, they are expected to possess a significant q parameter. This does not seem to be the case with Sagittarius A* for which a very strict upper bound of

$q \leq 8.6 \times 10^{-11}$ has been derived [129, 130].

VII. CONCLUSIONS

The recent publication of black hole images by the EHT collaboration gave rise to a novel way to probe the near horizon regime of black holes that is a valuable and complementary way to test deviations from GR. The data available by the EHT display a bright ring of emission which surrounds a dark depression that is roughly the size of the black hole shadow. In order to connect the size of the bright ring to the underlying shadow, one has to use the mass-to-distance ratio which for the supermassive black hole in the center of our galaxy SgrA* is much more accurately known compared to the previously available M87* due to the proximity of SgrA* to the Earth. For this reason, the bounds presented in the recent EHT publication [97] are the strongest to date regarding black hole metric deviations from GR in the near horizon regime from black hole imaging. In this work, we used these bounds in order to constrain a number of selected theories of modified gravity whose overarching theme is that they predict the existence of black holes bestowed with non-trivial scalar field profiles.

As there is no clear consensus yet on the spin parameter of Sagittarius A*, we limited our analysis to the spherically symmetric case. For this particular case, the deviation of the black hole metric from the Schwarzschild scenario is quantified by the fractional deviation δ whose bounds were announced in [97] and recreated in the present work in Table I. Among the various choices displayed in the Table, we settled with displaying the results of the image-domain feature extraction procedure *eht-imaging* and the fitting to the analytic model *mG-ring*. Our choices were motivated by the fact that these two constraints represent two very distinct methodologies. In addition, they lie at the two extremes of the spectrum of possible results, with the *eht-imaging* constraints being the most conservative ones allowing only for small deviations from GR and the *mG-ring* constraints being the most liberal ones favouring much larger deviations from GR.

Regarding the theories under consideration, we first focused on EsGB theory which is a well motivated modification of GR that involves higher curvature terms. Our focus in section IV was to study generic black holes with non-trivial scalar hair that are regular from the horizon to infinity and for several different choices for the scalar coupling function. We found that, for the linear coupling, the parameter space of the theory cannot be constrained by the EHT observations since the entire range of solutions are either all allowed by the *eht-imaging* constraint or excluded by the *mG-ring* constraints. However, for the quadratic and exponential couplings, we found a distinctly different behaviour of the solutions with positive and negative coupling parameter. The solutions derived for a positive coupling exhibit the same behaviour as in the linear coupling case with the whole set of solutions being allowed by the former EHT constraint and excluded by the latter. On the other hand, solutions with a negative coupling extend over a larger part of the parameter space and may thus be more ef-

fectively constrained by the EHT bounds. We also find that special solutions for which the energy momentum tensor component $T_r^r(r)$ can have a local maximum from the horizon to infinity can only occur for the quadratic coupling in a way that is consistent with the EHT results. In the context of this theory, we also highlighted differences in the shadows between black-holes and wormholes. However, a detailed analysis featuring wormhole solutions is left for future work.

Subsequently, in sections V-VI we turned our attention to spontaneous scalarization. We saw two different scenarios; in the first one scalarization is associated with the compactness of the object. In this case we examined in detail the effects on the shadow radius, from the couplings of a scalar field with curvature invariants (Ricci and GB). We saw that in principle the EHT can place significant constraints on the theory depending on the choices of the coupling parameters under examination. For the minimal EsRGB model we saw that there exists a small region in the parameter space of solutions that satisfies even the tightest combinations of the EHT bounds presented in Table I. If we also allow for higher order operator corrections in the EsGB coupling, then the allowed parameter space widens due to the fact that the minimal black-hole mass in this case is pushed towards zero.

Finally, in section VI we study scalarization as a result of a non-minimal coupling of a scalar field with the Maxwell tensor. Compared to the RN scenario, we were able to demonstrate that scalarized EMS black holes allow for agreement with the EHT bounds for a broader range of electric charges. Additionally, solutions are retrieved beyond the GR extremality limit with shadow radii within the desired bounds.

Looking to the future, the Next Generation EHT (ngEHT) project will provide us with significantly sharper images of the shadow of supermassive black holes such as M87* and SgrA* and also possibly real time video of the evolution of the accretion disk around the black hole horizon. This will usher a whole new era in fundamental physics in the strong gravity regime while giving birth to a whole new field: imaging and time resolution of black holes on horizon scales [131, 132]. It remains to be seen if the preference for a smaller black hole shadow than the one that is predicted in the Schwarzschild case will persist in the next generation of experiments.

ACKNOWLEDGEMENTS

This work was supported by IBS under the project code, IBS-R018-D1.

Appendix A: Equations in EsRGB theory

Here we present the equations of motion in the general-coupling case of the Einstein-scalar-Ricci-Gauss-Bonnet scenario, as this includes all of the cases considered in sections IV (by setting $h(\phi) = 0$) and V. The spherically symmetric ansatz we chose here has the following form:

$$ds^2 = -A(r)dt^2 + B(r)^{-1}dr^2 + r^2d\Omega^2. \quad (\text{A1})$$

For this ansatz, the two independent gravitational equations we use plus the scalar equation of motion read:

$$(t, t) : 16B^2(\dot{f}\phi'' + \ddot{f}\phi'^2) + B'[24B\dot{f}\phi' - 4(h+1)r - 2\phi'(4\dot{f} + \dot{h}r^2)] - B[r^2\phi'^2 + 16\dot{f}\phi'' + 16\ddot{f}\phi'^2 + 4r^2\dot{h}\phi'^2 + 4\dot{h}r(r\phi'' + 2\phi') + 4(h+1)] + 4(h+1) = 0, \quad (\text{A2})$$

$$(r, r) : 24B^2\dot{f}A'\phi' + B[-8\dot{f}A'\phi' - 2\dot{h}r^2A'\phi' - 4(h+1)rA' + Ar\phi'(r\phi' - 8\dot{h}) - 4A(h+1)] + 4A(h+1) = 0, \quad (\text{A3})$$

$$(\phi) : 2A^2Br^2\phi'' + 8AB^2\dot{f}A'' - 4A^2\dot{h}(rB' + B - 1) + \phi'(A^2r^2B' + 4A^2Br + ABr^2A') - 4AB\dot{h}rA' - 2ABA''(4\dot{f} + \dot{h}r^2) - AA'B'(4\dot{f} + \dot{h}r^2) + 12AB\dot{f}A'B' + BA'^2(\dot{h}r^2 - 4(B-1)\dot{f}) = 0. \quad (\text{A4})$$

Appendix B: Equations in EMS theory

For the EMS scalarization model discussed in VI, we use the following metric ansatz (in order to be consistent with [126, 127]):

$$ds^2 = -N(r)e^{-2\delta(r)}dt^2 + N(r)^{-1}dr^2 + r^2d\Omega^2 \quad (\text{B1})$$

where $N(r) = 1 - 2m(r)/r$, with $m(r)$ being the Misner-Sharp mass [133]. Then, the Einstein (tt and rr), scalar and electromagnetic equations (43)-(45) yield:

$$(t, t) : m' - \frac{1}{8}r^2\left(1 - \frac{2m}{r}\right)\phi'^2 + \frac{1}{2}e^{2\delta}r^2fV'^2 = 0, \quad (\text{B2})$$

$$(r, r) : 4\delta' + r\phi'^2 = 0, \quad (\text{B3})$$

$$(\phi) : 4r(r-2m)\phi'' + r^2(2m-r)\phi'^3 - 8e^{2\delta}r^2V'^2\dot{f} + 4[e^{2\delta}r^3fV'^2 + r\delta'(2m-r) - 2m + 2r]\phi' = 0, \quad (\text{B4})$$

$$(em) : r^2fV' - e^{-\delta}Q_e = 0. \quad (\text{B5})$$

It is then straightforward to solve with respect to m' and ϕ'' , which leaves with a system of ordinary differential equations that can be integrated. The appropriate boundary conditions are found by taking the near-horizon expansions of the functions m , ϕ , δ , V .

-
- [1] B. Bertotti, L. Iess, and P. Tortora, *Nature* **425**, 374 (2003).
[2] I. H. Stairs, *Living Rev. Rel.* **6**, 5 (2003), arXiv:astro-ph/0307536.
[3] A. Verma, A. Fienga, J. Laskar, H. Manche, and M. Gastineau, *Astron. Astrophys.* **561**, A115 (2014), arXiv:1306.5569 [astro-ph.EP].
[4] S. B. Lambert and C. Le Poncin-Lafitte, *Astron. Astrophys.* **529**, A70 (2011).
[5] C. M. Will, *Living Rev. Rel.* **17**, 4 (2014), arXiv:1403.7377 [gr-qc].
[6] M. Kramer *et al.*, *Phys. Rev. X* **11**, 041050 (2021), arXiv:2112.06795 [astro-ph.HE].
[7] H. Luckoek and I. Moss, *Phys. Lett. B* **176**, 341 (1986).
[8] P. Bizon, *Phys. Rev. Lett.* **64**, 2844 (1990).
[9] B. A. Campbell, M. J. Duncan, N. Kaloper, and K. A. Olive, *Phys. Lett. B* **251**, 34 (1990).
[10] B. A. Campbell, N. Kaloper, and K. A. Olive, *Phys. Lett. B* **285**, 199 (1992).
[11] K.-I. Maeda, T. Tachizawa, T. Torii, and T. Maki, *Phys. Rev. Lett.* **72**, 450 (1994), arXiv:gr-qc/9310015.
[12] P. Kanti, N. E. Mavromatos, J. Rizos, K. Tamvakis, and E. Winstanley, *Phys. Rev. D* **54**, 5049 (1996), arXiv:hep-th/9511071.
[13] P. Kanti and K. Tamvakis, *Phys. Lett. B* **392**, 30 (1997), arXiv:hep-th/9609003.
[14] P. Kanti, N. E. Mavromatos, J. Rizos, K. Tamvakis, and E. Winstanley, *Phys. Rev. D* **57**, 6255 (1998), arXiv:hep-th/9703192.
[15] T. Torii, H. Yajima, and K.-i. Maeda, *Phys. Rev. D* **55**, 739 (1997), arXiv:gr-qc/9606034.
[16] R. P. Kerr, *Phys. Rev. Lett.* **11**, 237 (1963).
[17] W. Israel, *Phys. Rev.* **164**, 1776 (1967).
[18] W. Israel, *Commun. Math. Phys.* **8**, 245 (1968).
[19] B. Carter, *Phys. Rev.* **174**, 1559 (1968).
[20] B. Carter, *Phys. Rev. Lett.* **26**, 331 (1971).
[21] S. W. Hawking, *Commun. Math. Phys.* **25**, 152 (1972).
[22] R. H. Price, *Phys. Rev. D* **5**, 2419 (1972).
[23] R. H. Price, *Phys. Rev. D* **5**, 2439 (1972).
[24] D. C. Robinson, *Phys. Rev. Lett.* **34**, 905 (1975).
[25] C. Teitelboim, *Phys. Rev. D* **5**, 2941 (1972).
[26] J. D. Bekenstein, *Phys. Rev. D* **5**, 1239 (1972).
[27] J. D. Bekenstein, *Phys. Rev. D* **5**, 2403 (1972).
[28] J. D. Bekenstein, *Phys. Rev. D* **51**, R6608 (1995).
[29] Z.-K. Guo, N. Ohta, and T. Torii, *Prog. Theor. Phys.* **120**, 581 (2008), arXiv:0806.2481 [gr-qc].
[30] P. Pani and V. Cardoso, *Phys. Rev. D* **79**, 084031 (2009), arXiv:0902.1569 [gr-qc].
[31] P. Pani, C. F. B. Macedo, L. C. B. Crispino, and V. Cardoso, *Phys. Rev. D* **84**, 087501 (2011), arXiv:1109.3996 [gr-qc].
[32] B. Kleihaus, J. Kunz, and E. Radu, *Phys. Rev. Lett.* **106**, 151104 (2011), arXiv:1101.2868 [gr-qc].
[33] K. Yagi, N. Yunes, and T. Tanaka, *Phys. Rev. D* **86**, 044037 (2012), [Erratum: *Phys. Rev. D* **89**, 049902 (2014)], arXiv:1206.6130 [gr-qc].
[34] T. P. Sotiriou and S.-Y. Zhou, *Phys. Rev. Lett.* **112**, 251102 (2014), arXiv:1312.3622 [gr-qc].
[35] T. P. Sotiriou and S.-Y. Zhou, *Phys. Rev. D* **90**, 124063 (2014), arXiv:1408.1698 [gr-qc].
[36] B. Kleihaus, J. Kunz, S. Mojica, and E. Radu, *Phys. Rev. D* **93**, 044047 (2016), arXiv:1511.05513 [gr-qc].
[37] J. L. Blázquez-Salcedo, C. F. B. Macedo, V. Cardoso, V. Ferrari, L. Gualtieri, F. S. Khoo, J. Kunz, and P. Pani, *Phys. Rev.*

- D **94**, 104024 (2016), arXiv:1609.01286 [gr-qc].
- [38] G. Antoniou, A. Bakopoulos, and P. Kanti, *Phys. Rev. Lett.* **120**, 131102 (2018), arXiv:1711.03390 [hep-th].
- [39] G. Antoniou, A. Bakopoulos, and P. Kanti, *Phys. Rev. D* **97**, 084037 (2018), arXiv:1711.07431 [hep-th].
- [40] D. D. Doneva and S. S. Yazadjiev, *Phys. Rev. Lett.* **120**, 131103 (2018), arXiv:1711.01187 [gr-qc].
- [41] H. O. Silva, J. Sakstein, L. Gualtieri, T. P. Sotiriou, and E. Berti, *Phys. Rev. Lett.* **120**, 131104 (2018), arXiv:1711.02080 [gr-qc].
- [42] Y. Brihaye, B. Hartmann, and J. Urrestilla, *JHEP* **06**, 074 (2018), arXiv:1712.02458 [gr-qc].
- [43] D. D. Doneva, S. Kiorpelidi, P. G. Nedkova, E. Papantonopoulos, and S. S. Yazadjiev, *Phys. Rev. D* **98**, 104056 (2018), arXiv:1809.00844 [gr-qc].
- [44] A. Bakopoulos, G. Antoniou, and P. Kanti, *Phys. Rev. D* **99**, 064003 (2019), arXiv:1812.06941 [hep-th].
- [45] H. Witek, L. Gualtieri, P. Pani, and T. P. Sotiriou, *Phys. Rev. D* **99**, 064035 (2019), arXiv:1810.05177 [gr-qc].
- [46] M. Minamitsuji and T. Ikeda, *Phys. Rev. D* **99**, 044017 (2019), arXiv:1812.03551 [gr-qc].
- [47] C. F. B. Macedo, J. Sakstein, E. Berti, L. Gualtieri, H. O. Silva, and T. P. Sotiriou, *Phys. Rev. D* **99**, 104041 (2019), arXiv:1903.06784 [gr-qc].
- [48] D. D. Doneva, K. V. Staykov, and S. S. Yazadjiev, *Phys. Rev. D* **99**, 104045 (2019), arXiv:1903.08119 [gr-qc].
- [49] D.-C. Zou and Y. S. Myung, *Phys. Rev. D* **100**, 124055 (2019), arXiv:1909.11859 [gr-qc].
- [50] P. V. P. Cunha, C. A. R. Herdeiro, and E. Radu, *Phys. Rev. Lett.* **123**, 011101 (2019), arXiv:1904.09997 [gr-qc].
- [51] Y. Brihaye, B. Hartmann, N. P. Aprile, and J. Urrestilla, *Phys. Rev. D* **101**, 124016 (2020), arXiv:1911.01950 [gr-qc].
- [52] K. A. Bronnikov, *Acta Phys. Polon. B* **4**, 251 (1973).
- [53] H. G. Ellis, *J. Math. Phys.* **14**, 104 (1973).
- [54] M. Visser, S. Kar, and N. Dadhich, *Phys. Rev. Lett.* **90**, 201102 (2003), arXiv:gr-qc/0301003.
- [55] K. A. Bronnikov, *Grav. Cosmol.* **2**, 221 (1996), arXiv:gr-qc/9703020.
- [56] K. A. Bronnikov and J. C. Fabris, *Class. Quant. Grav.* **14**, 831 (1997), arXiv:gr-qc/9603037.
- [57] C. Armendariz-Picon, *Phys. Rev. D* **65**, 104010 (2002), arXiv:gr-qc/0201027.
- [58] K. A. Bronnikov and S. V. Grinyok, *Grav. Cosmol.* **10**, 237 (2004), arXiv:gr-qc/0411063.
- [59] F. S. N. Lobo, *Phys. Rev. D* **71**, 084011 (2005), arXiv:gr-qc/0502099.
- [60] F. S. N. Lobo, *Phys. Rev. D* **73**, 064028 (2006), arXiv:gr-qc/0511003.
- [61] F. S. N. Lobo and M. A. Oliveira, *Phys. Rev. D* **80**, 104012 (2009), arXiv:0909.5539 [gr-qc].
- [62] K. A. Bronnikov, M. V. Skvortsova, and A. A. Starobinsky, *Grav. Cosmol.* **16**, 216 (2010), arXiv:1005.3262 [gr-qc].
- [63] N. M. Garcia and F. S. N. Lobo, *Phys. Rev. D* **82**, 104018 (2010), arXiv:1007.3040 [gr-qc].
- [64] P. Kanti, B. Kleihaus, and J. Kunz, *Phys. Rev. Lett.* **107**, 271101 (2011), arXiv:1108.3003 [gr-qc].
- [65] P. Kanti, B. Kleihaus, and J. Kunz, *Phys. Rev. D* **85**, 044007 (2012), arXiv:1111.4049 [hep-th].
- [66] S. V. Bolokhov, K. A. Bronnikov, and M. V. Skvortsova, *Class. Quant. Grav.* **29**, 245006 (2012), arXiv:1208.4619 [gr-qc].
- [67] K. A. Bronnikov and A. M. Galiakhmetov, *Grav. Cosmol.* **21**, 283 (2015), arXiv:1508.01114 [gr-qc].
- [68] R. Shaikh, *Phys. Rev. D* **92**, 024015 (2015), arXiv:1505.01314 [gr-qc].
- [69] M. R. Mehdizadeh, M. Kord Zangeneh, and F. S. N. Lobo, *Phys. Rev. D* **91**, 084004 (2015), arXiv:1501.04773 [gr-qc].
- [70] P. K. F. Kuhfittig, *Indian J. Phys.* **92**, 1207 (2018), arXiv:1801.10474 [gr-qc].
- [71] R. Ibadov, B. Kleihaus, J. Kunz, and S. Murodov, (2021), arXiv:2111.09628 [gr-qc].
- [72] T. Karakasis, E. Papantonopoulos, and C. Vlachos, *Phys. Rev. D* **105**, 024006 (2022), arXiv:2107.09713 [gr-qc].
- [73] B. Ghosh and S. Mitra, *Int. J. Mod. Phys. A* **36**, 18 (2021), arXiv:2108.12670 [gr-qc].
- [74] I. Z. Fisher, *Zh. Eksp. Teor. Fiz.* **18**, 636 (1948), arXiv:gr-qc/9911008.
- [75] A. I. Janis, E. T. Newman, and J. Winicour, *Phys. Rev. Lett.* **20**, 878 (1968).
- [76] M. Wyman, *Phys. Rev. D* **24**, 839 (1981).
- [77] A. G. Agnese and M. La Camera, *Phys. Rev. D* **31**, 1280 (1985).
- [78] M. D. Roberts, *Gen. Rel. Grav.* **21**, 907 (1989).
- [79] B. Kleihaus, J. Kunz, and P. Kanti, *Phys. Lett. B* **804**, 135401 (2020), arXiv:1910.02121 [gr-qc].
- [80] B. Kleihaus, J. Kunz, and P. Kanti, *Phys. Rev. D* **102**, 024070 (2020), arXiv:2005.07650 [gr-qc].
- [81] B. P. Abbott *et al.* (LIGO Scientific, Virgo), *Phys. Rev. Lett.* **116**, 061102 (2016), arXiv:1602.03837 [gr-qc].
- [82] B. P. Abbott *et al.* (LIGO Scientific, Virgo), *Phys. Rev. Lett.* **119**, 161101 (2017), arXiv:1710.05832 [gr-qc].
- [83] R. Abbott *et al.* (LIGO Scientific, Virgo), (2020), arXiv:2010.14527 [gr-qc].
- [84] K. Akiyama *et al.* (Event Horizon Telescope), *Astrophys. J. Lett.* **875**, L1 (2019), arXiv:1906.11238 [astro-ph.GA].
- [85] K. Akiyama *et al.* (Event Horizon Telescope), *Astrophys. J. Lett.* **875**, L2 (2019), arXiv:1906.11239 [astro-ph.IM].
- [86] K. Akiyama *et al.* (Event Horizon Telescope), *Astrophys. J. Lett.* **875**, L3 (2019), arXiv:1906.11240 [astro-ph.GA].
- [87] K. Akiyama *et al.* (Event Horizon Telescope), *Astrophys. J. Lett.* **875**, L4 (2019), arXiv:1906.11241 [astro-ph.GA].
- [88] K. Akiyama *et al.* (Event Horizon Telescope), *Astrophys. J. Lett.* **875**, L5 (2019), arXiv:1906.11242 [astro-ph.GA].
- [89] K. Akiyama *et al.* (Event Horizon Telescope), *Astrophys. J. Lett.* **875**, L6 (2019), arXiv:1906.11243 [astro-ph.GA].
- [90] K. Akiyama *et al.* (Event Horizon Telescope), *Astrophys. J. Lett.* **910**, L12 (2021), arXiv:2105.01169 [astro-ph.HE].
- [91] K. Akiyama *et al.* (Event Horizon Telescope), *Astrophys. J. Lett.* **910**, L13 (2021), arXiv:2105.01173 [astro-ph.HE].
- [92] K. Akiyama *et al.* (Event Horizon Telescope), *Astrophys. J. Lett.* **930**, L12 (2022).
- [93] K. Akiyama *et al.* (Event Horizon Telescope), *Astrophys. J. Lett.* **930**, L13 (2022).
- [94] K. Akiyama *et al.* (Event Horizon Telescope), *Astrophys. J. Lett.* **930**, L14 (2022).
- [95] K. Akiyama *et al.* (Event Horizon Telescope), *Astrophys. J. Lett.* **930**, L15 (2022).
- [96] K. Akiyama *et al.* (Event Horizon Telescope), *Astrophys. J. Lett.* **930**, L16 (2022).
- [97] K. Akiyama *et al.* (Event Horizon Telescope), *Astrophys. J. Lett.* **930**, L17 (2022).
- [98] D. Psaltis *et al.* (Event Horizon Telescope), *Phys. Rev. Lett.* **125**, 141104 (2020), arXiv:2010.01055 [gr-qc].
- [99] P. Kocherlakota *et al.* (Event Horizon Telescope), *Phys. Rev. D* **103**, 104047 (2021), arXiv:2105.09343 [gr-qc].
- [100] S. Vagnozzi, R. Roy, Y.-D. Tsai, and L. Visinelli, (2022), arXiv:2205.07787 [gr-qc].

- [101] H. Falcke, F. Melia, and E. Agol, *Astrophys. J. Lett.* **528**, L13 (2000), arXiv:astro-ph/9912263.
- [102] R. Abuter *et al.* (GRAVITY), *Astron. Astrophys.* **615**, L15 (2018), arXiv:1807.09409 [astro-ph.GA].
- [103] A. Amorim *et al.* (GRAVITY), *Phys. Rev. Lett.* **122**, 101102 (2019), arXiv:1902.04193 [astro-ph.GA].
- [104] R. Abuter *et al.* (GRAVITY), *Astron. Astrophys.* **636**, L5 (2020), arXiv:2004.07187 [astro-ph.GA].
- [105] T. Do *et al.*, *Science* **365**, 664 (2019), arXiv:1907.10731 [astro-ph.GA].
- [106] A. Hees, A. Dehghanfar, T. Do, A. M. Ghez, G. D. Martinez, R. Campbell, and J. R. Lu, *Astrophys. J.* **880**, 87 (2019), arXiv:1906.03099 [astro-ph.IM].
- [107] R. Della Monica, I. de Martino, and M. de Laurentis, *Mon. Not. Roy. Astron. Soc.* **510**, 4757 (2022), arXiv:2105.12687 [gr-qc].
- [108] I. de Martino, R. della Monica, and M. de Laurentis, *Phys. Rev. D* **104**, L101502 (2021), arXiv:2106.06821 [gr-qc].
- [109] G. Fragione and A. Loeb, *Astrophys. J. Lett.* **932**, L17 (2022), arXiv:2205.12274 [astro-ph.GA].
- [110] D. Psaltis, *Phys. Rev. D* **77**, 064006 (2008), arXiv:0704.2426 [astro-ph].
- [111] G. Antoniou, A. Bakopoulos, P. Kanti, B. Kleihaus, and J. Kunz, *Phys. Rev. D* **101**, 024033 (2020), arXiv:1904.13091 [hep-th].
- [112] H. G. Ellis, *J. Math. Phys.* **14**, 104 (1973).
- [113] K. A. Bronnikov, *Acta Phys. Polon. B* **4**, 251 (1973).
- [114] V. Perlick and O. Y. Tsupko, *Phys. Rept.* **947**, 1 (2022), arXiv:2105.07101 [gr-qc].
- [115] B.-H. Lee, W. Lee, and D. Ro, *Phys. Rev. D* **99**, 024002 (2019), arXiv:1809.05653 [gr-qc].
- [116] A. Papageorgiou, C. Park, and M. Park, *Phys. Rev. D* **106**, 084024 (2022), arXiv:2205.00907 [hep-th].
- [117] S. E. Perkins, R. Nair, H. O. Silva, and N. Yunes, *Phys. Rev. D* **104**, 024060 (2021), arXiv:2104.11189 [gr-qc].
- [118] J. L. Blázquez-Salcedo, D. D. Doneva, J. Kunz, and S. S. Yazadjiev, *Phys. Rev. D* **98**, 084011 (2018), arXiv:1805.05755 [gr-qc].
- [119] G. Antoniou, C. F. B. Macedo, R. McManus, and T. P. Sotiriou, *Phys. Rev. D* **106**, 024029 (2022), arXiv:2204.01684 [gr-qc].
- [120] N. Andreou, N. Franchini, G. Ventagli, and T. P. Sotiriou, *Phys. Rev. D* **99**, 124022 (2019), [Erratum: *Phys. Rev. D* **101**, 109903 (2020)], arXiv:1904.06365 [gr-qc].
- [121] H. O. Silva, C. F. B. Macedo, T. P. Sotiriou, L. Gualtieri, J. Sakstein, and E. Berti, *Phys. Rev. D* **99**, 064011 (2019), arXiv:1812.05590 [gr-qc].
- [122] G. Ventagli, A. Lehébel, and T. P. Sotiriou, *Phys. Rev. D* **102**, 024050 (2020), arXiv:2006.01153 [gr-qc].
- [123] G. Antoniou, L. Bordin, and T. P. Sotiriou, *Phys. Rev. D* **103**, 024012 (2021), arXiv:2004.14985 [gr-qc].
- [124] G. Ventagli, G. Antoniou, A. Lehébel, and T. P. Sotiriou, *Phys. Rev. D* **104**, 124078 (2021), arXiv:2111.03644 [gr-qc].
- [125] G. Antoniou, A. Lehébel, G. Ventagli, and T. P. Sotiriou, *Phys. Rev. D* **104**, 044002 (2021), arXiv:2105.04479 [gr-qc].
- [126] C. A. R. Herdeiro, E. Radu, N. Sanchis-Gual, and J. A. Font, *Phys. Rev. Lett.* **121**, 101102 (2018), arXiv:1806.05190 [gr-qc].
- [127] P. G. S. Fernandes, C. A. R. Herdeiro, A. M. Pombo, E. Radu, and N. Sanchis-Gual, *Class. Quant. Grav.* **36**, 134002 (2019), [Erratum: *Class. Quant. Grav.* **37**, 049501 (2020)], arXiv:1902.05079 [gr-qc].
- [128] J. L. Blázquez-Salcedo, C. A. R. Herdeiro, J. Kunz, A. M. Pombo, and E. Radu, *Phys. Lett. B* **806**, 135493 (2020), arXiv:2002.00963 [gr-qc].
- [129] M. Zajaček, A. Tursunov, A. Eckart, and S. Britzen, *Mon. Not. Roy. Astron. Soc.* **480**, 4408 (2018), arXiv:1808.07327 [astro-ph.GA].
- [130] M. Zajaček, A. Tursunov, A. Eckart, S. Britzen, E. Hackmann, V. Karas, Z. Stuchlík, B. Czerny, and J. A. Zensus, *J. Phys. Conf. Ser.* **1258**, 012031 (2019), arXiv:1812.03574 [astro-ph.GA].
- [131] L. Blackburn *et al.*, (2019), arXiv:1909.01411 [astro-ph.IM].
- [132] S. Doeleman, in *American Astronomical Society Meeting Abstracts*, American Astronomical Society Meeting Abstracts, Vol. 53 (2021) p. 221.01.
- [133] C. W. Misner and D. H. Sharp, *Phys. Rev.* **136**, B571 (1964).